International Journal of Solids and Structures 256 (2022) 111983

Contents lists available at ScienceDirect

International Journal of Solids and Structures

journal homepage: www.elsevier.com/locate/ijsolstr

An atomistic entropy based finite element multiscale method for modeling amorphous materials

Hesam Moslemzadeh, Soheil Mohammadi *

High Performance Computing Laboratory, School of Civil Engineering, Faculty of Engineering, University of Tehran, Tehran, Iran

ARTICLE INFO

Keywords:
Multiscale modeling
Amorphous materials
Meshless methods
Maximum entropy

ABSTRACT

A new concurrent multiscale method based on the maximum entropy statistical method is proposed for the analysis of amorphous materials. In addition to reducing the number of degrees of freedom, any irregular structure of amorphous materials can be accurately analyzed. The amorphous structure is generated from a solid crystalline structure by a heating/cooling process without the need for any specific independent technique to create such a random structure. The method is expected to perform efficiently because of its entropic and irregular intrinsic. Regions with moderate conditions are discretized by the entropy-based finite element method while the severe parts are simulated by the present atomistic-based multiscale technique. The new proposed approach allows for accurate analysis of amorphous structures across multiple scales and does not suffer from conventional complications such as the standard Cauchy Born rule and consistency of the molecular structure with the standard finite element geometries.

The conventional Cauchy-Born rule cannot be directly used due to the non–crystalline microstructure of the material. A remedy is proposed based on the meshfree techniques by constructing a continuous atomic deformation field from the imposed macro deformation gradient. The resultant deformation gradient and the stress field remain consistent in micro scales. In addition, a genetic algorithm-based method, which has less sensitivity to the choice of initial point and number of parameters, is adopted for the maximization of the entropy function.

The silicon amorphous structure is considered for MD simulations. It is obtained by quenching from a melted sample. The MD-obtained structure is further analyzed and the predicted displacements and stress contours, as well as the density and radial distribution functions are examined to assess the state of the material. Then, the proposed meshfree technique is applied to construct the continuous form of the deformation gradient on the MD model to improve the accuracy of the solution. The proposed concurrent multiscale method is verified and then employed to simulate an amorphous silicon specimen. Finally, the effects of sample size, strain rate and quenching speed on rupture stress and strain in different 3D tensile simulations are investigated by the proposed multiscale method.

1. Introduction

Experimental and numerical studies of the structure of materials have been frequently reported in recent years in order to determine their mechanical characteristics. Due to the large demand for the production of new materials with complex structures and their application under extreme loading conditions, more attention have been directed towards the development of novel and efficient computational methods to allow for accurate simulations of such complicated problems.

Depending on their structure, metals have regular structural patterns that include crystal-like repetitive molecular configurations. In contrast, there are other materials with less or no repetitive structural patterns, such as polycrystallines, polymers and amorphous metals (see Fig. 1). In recent years, the use of these materials, especially amorphous materials, has grown significantly due to their distinct mechanical and chemical properties. For instance, they can be used as high-strength structural glasses (Rinaldi et al., 2011), hydrated cement in the processing of concrete (Hufnagel et al., 2016), coating materials (Joshi et al., 2015; Liu and Zhang, 2014; Wang et al., 2016; Wang et al., 2017), fillers (Kahn et al., 1995), and amorphous polymer elastomers in structural separators (Milani and Milani, 2014; Mouton, 2013; Mouton, 2013). Given the increasing use of these materials and their unique properties in high-

* Corresponding author.
E-mail address: smoham@ut.ac.ir (S. Mohammadi).

https://doi.org/10.1016/j.ijsolstr.2022.111983
Received 11 April 2022; Received in revised form 26 July 2022; Accepted 22 September 2022
Available online 26 September 2022

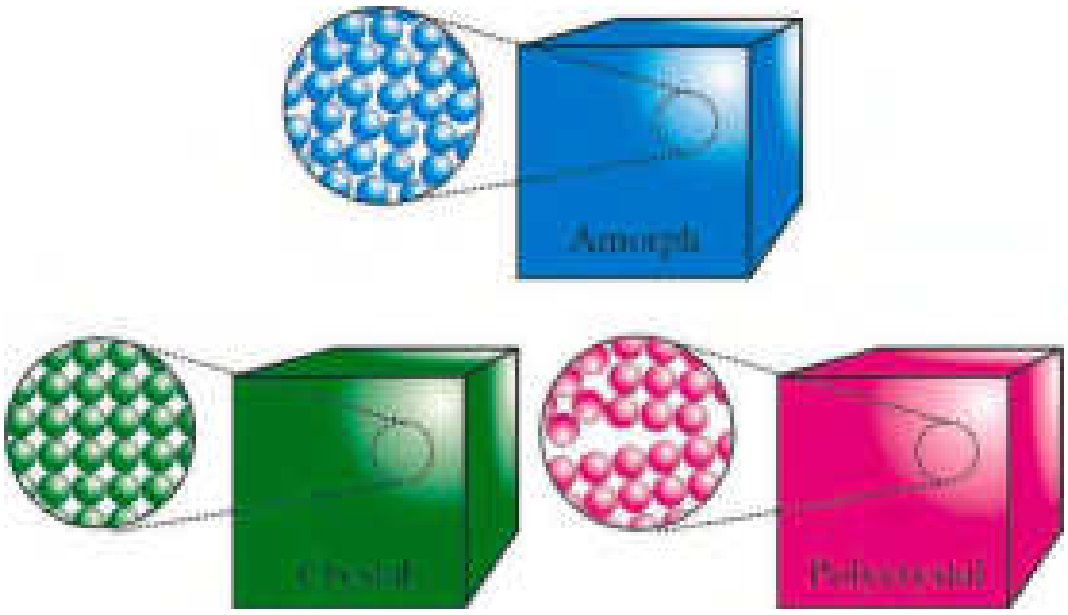

Fig. 1. Different atomic structures.

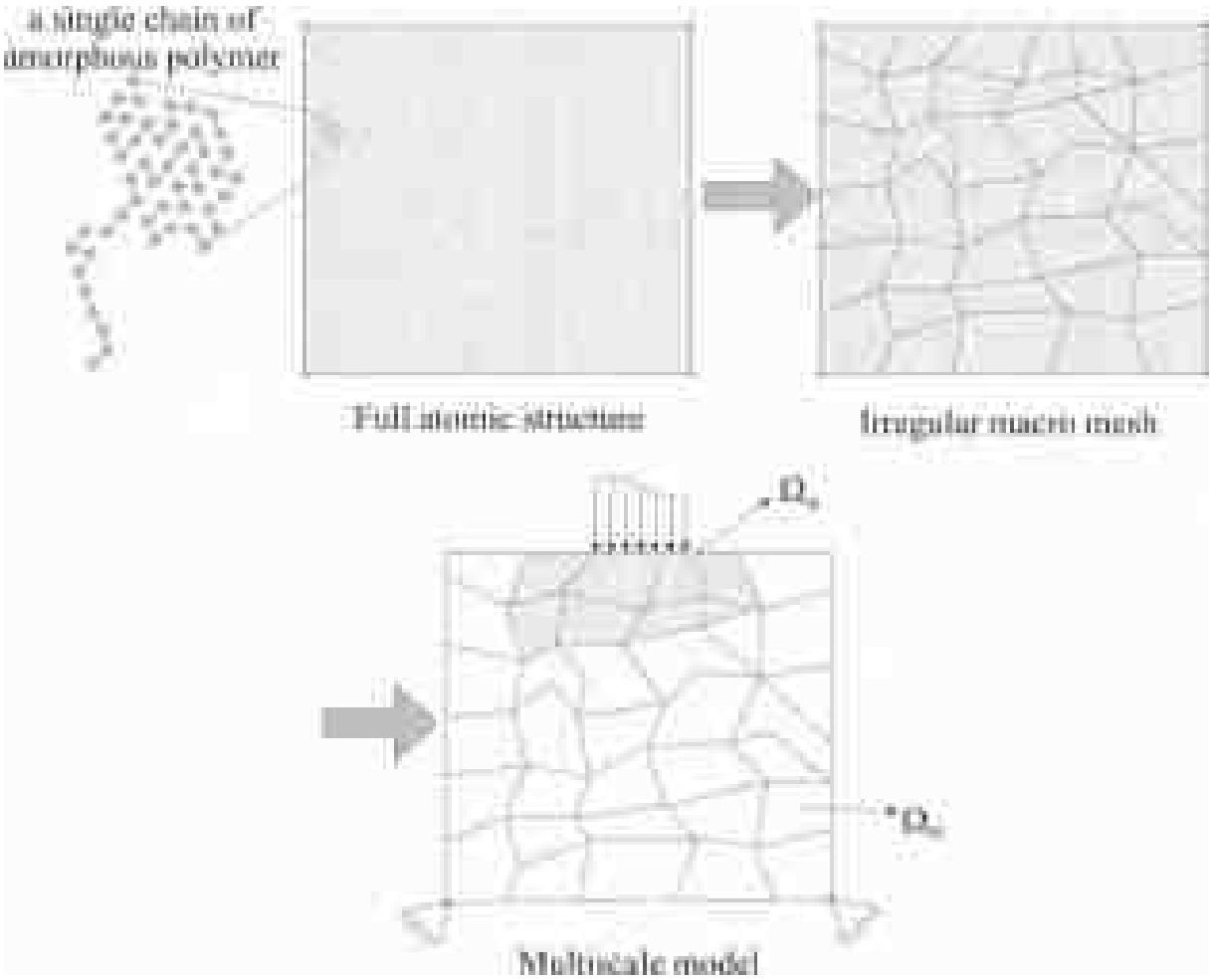

Fig. 2. Schematic model of the micro Ω_m and macro Ω_M regions.

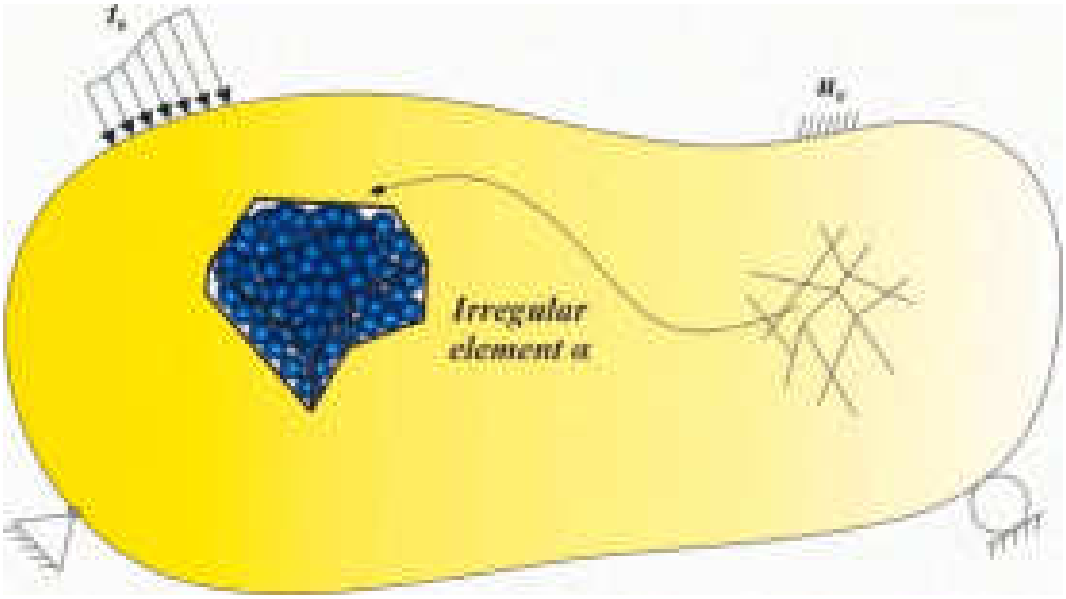

Fig. 3. An amorphous silicon structure within a typical irregular element α.

Table 1
Parameters of the employed genetic algorithm.

Population (size)	Real valued (100)
Selection	Stochastic uniform
Elite count	2
Cross over	Heuristic
Mutation	Adaptive feasible
Stopping criterion	10^{-10}

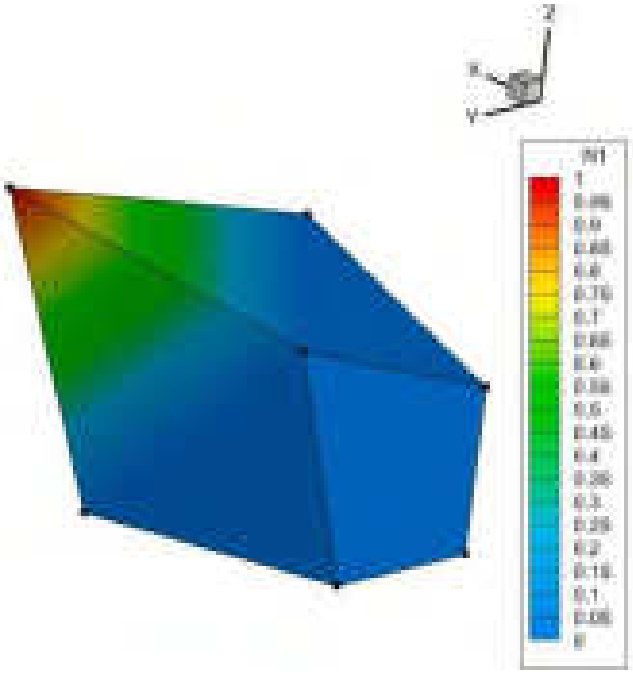

Fig. 4. A typical contour of entropy-based shape function for an irregular 3D element.

tech industries, the need for accurate modeling and analysis is crucial to determine their properties and to accurately predict their behavior under various loading conditions.

Considering the complexity of the structure of these materials, a novel computational method is developed and implemented in order to take advantage of entropy-based concepts in a multiscale method to accurately simulate the response of amorphous materials. In the following, the existing methods of analysis of amorphous materials are briefly reviewed and the corresponding multi-scale methods are explained. More emphasis is placed on the concurrent multiscale methods. Moreover, the statistical formulation of the maximum entropy is reviewed and further details of the proposed multiscale method are presented.

Accurate modeling of nano-scale materials has been frequently performed with molecular dynamics to obtain their basic properties. For instance, Abdolhosseini Qomi et al. (2014) studied different proportions of the amorphous calcium silicate hydrate to optimize the properties of cement. They examined a set of mechanical properties such as modulus of elasticity and hardness in the indentation process. Bauchy (2017) simulated the atomic structure of cement and concrete with the help of springs and trusses and studied their hardness, toughness and creep. They used X-ray scan results to study the irregular structure of calcium hydrate silicate. In another study, Bauchy et al. (2015) obtained the brittle properties of calcium hydrate silicate structure by molecular dynamics to determine the increase of ductility with a decreasing ratio of calcium to silicate.

Fan et al. (2009) introduced a new concept of interatomic free space and studied the amorphous structure of glass metals using atomic simulations to investigate the formation of shear bands and their high strengths at different temperatures. This concept was different from the free space defined in hard atomic sphere models of crystals based on separate stable clusters with interconnecting zones. The effects of strain rate on compression tests and the cooling rate on strain localization were studied by Shi and Falk (2006). Moreover, they performed shear band modeling of frictionless indentation of an amorphous film under different boundary conditions by three-dimensional atomic modeling of amorphous glasses (Shi and Falk, 2007).

Falk and Maloney studied elasticity, plasticity and fracture properties of amorphous materials by molecular simulation and Huffenel et al. reviewed the structural theories of glass metals (Hufnagel et al., 2016; Falk and Maloney, 2010). Also, Falk and Langer examined the fracture response of these materials by shear transition theories (Falk and Langer, 2011). Demetriou et al. (2009) modeled shear bands in the deformation of amorphous materials using a large-scale method and

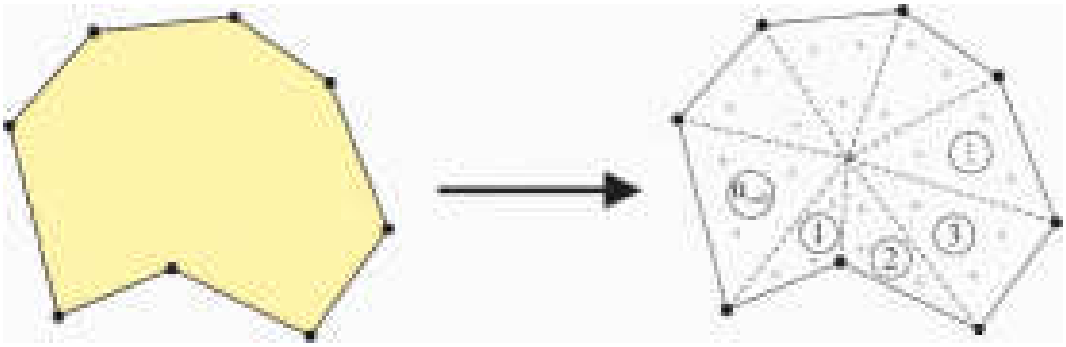

Fig. 5. Division of a concave element into n_{cell} smaller convex cells and the corresponding integration points.

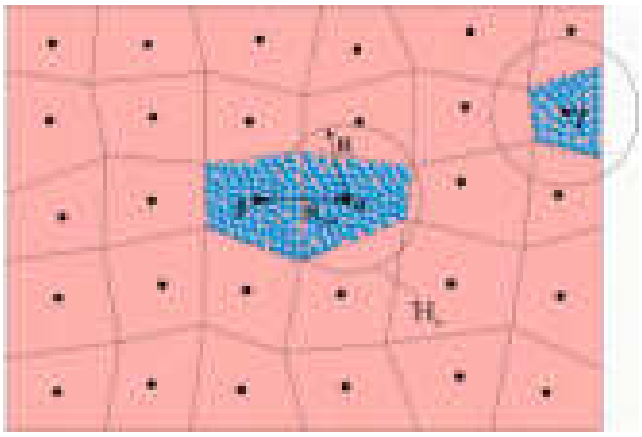

Fig. 6. Definition of neighbor elements β and a typical surface edge element.

Park et al. (2014) adopted the same method to determine the adhesive area on the interface.

Macroscale methods, such as the finite element method, have also been used for modeling amorphous materials. Park et al. (2007) adopted FEM to investigate the effect of volume percentage on the mechanical properties of amorphous copper with crystalline copper coatings, including fracture ductility. They concluded that the volume percentage would play an effective role in the strain–stress response of these materials, leading to a brittle failure in lower volume ratios. Linear and nonlinear modelings of amorphous materials were conducted by the commercial finite element software Abaqus by Rinaldi et al. (Rinaldi et al., 2011; Rinaldi et al., 2011). They used quasi-point defect theory to study softening, large deformation, and various mechanical responses of amorphous glassy polymers at different temperatures. They introduced disordered structural units in interaction with their close neighborhoods in the length order of the repeated unit cells, to capture irregularities by quasi-point defects. Moreover, they determined the viscoelastic modulus of composites with short glass fibers and investigated the effect of orientation of constituent fibers. The irregular structure of fibers was generated by the random Mont Carlo model (Gusev, 2017).

Timel et al. employed shell elements for glass and interlayer reinforcement membranes to model impact-resistant glasses and compared the experimental results with finite element simulations (Timmel et al., 2007). Holopanen et al. proposed a model based on the fatigue of polymer glasses under cyclic axial loads (Holopainen, 2014; Holopainen et al., 2017). They used lattice structures to evaluate the growth of voids in these materials under large deformations and studied their hardness, softening and plastic instability under non-uniform loadings (Holopainen, 2013). Moreover, Foyouzat et al. studied the fracture behavior of amorphous shape memory polymers (SMPs) using a phase transition-based constitutive model within an XFEM methodology (Foyouzat et al., 2020, 2021). They also examined the fracture parameters in two common thermomechanical loading cycles, namely, stress-free- strain recovery and fixed strain–stress recovery processes (Foyouzat et al., 2021).

In view of the fact that macroscale modelings provide less accuracy compared with microscale simulations, especially in situations where the material is subjected to severe conditions, multiscale methods constitute powerful alternatives to combine the efficiency of macroscale methods and the accuracy of atomistic-scale modelings (Alizadeh and Mohammadi, 2019; Fish, 2010; Fish and Yu, 2001; Tadmor and Miller, 2011; Wagner and Liu, 2003; Xiao and Belytschko, 2004). Nowadays, several multiscale simulations have been developed and applied to different engineering problems by both the concurrent schemes (Alizadeh et al., 2016; Kochmann and Amelang, 2016; Shenoy et al., 1999; Tadmor et al., 1996; Moslemzadeh et al., 2019) and the hierarchal methods (Bayesteh and Mohammadi, 2017; Forest, 2002; Hassani and Hinton, 1998; Hassani and Hinton, 1998; Dehaghani et al., 2017). These approaches differ in the type and number of degrees of freedom, the level of accuracy, and the way by which the regions and scales are connected. Talebi et al. (2014) reviewed hierarchical, semi concurrent, and concurrent multiscale methods and presented a multiscale framework for simulating cracks in solids. Bansal et al. proposed a multi-split element for 3D modeling of materials with uniform and non-uniform distributions of heterogeneity (Bansal et al., 2019). Furthermore, Nguyen et al. employed an X-ray scan for multiscale modeling of the foamed concrete and showed that the interconnection between pores plays a key role in the failure of concrete (Nguyen et al., 2018). For predicting the effect of parameters on results, a deep high-order neural network approach was employed by Nguyen et al. to predict the mechanical properties of foamed concrete (Nguyen et al., 2019). Moreover, to deal with errors and uncertainties of experimental and numerical data, the probabilistic identification of mechanical properties of materials was performed by Rappel et al. using a Bayesian inference to improve the results (Rappel et al., 2019; Rappel et al., 1606).

Beyond the conventional techniques, Hauseux et al. adopted coupled quantum physics and continuum mechanics to treat the Van Der Waals interactions in the chains of carbon and delamination of graphene from a silicon substrate (Hauseux et al., 2020; Hauseux et al., 2106). Besides, reduced order techniques based on low-dimensional subspaces were employed by Kerfriden et al. for multiscale modeling of crack initiation (Kerfriden et al., 2012; Kerfriden et al., 2011) and crack propagation (Kerfriden et al., 2013).

Within the context of multiscale simulations of amorphous materials, Su et al. presented a concurrent three-dimensional multiscale method based on element deformation modes (Su et al., 2012). They employed a linear mapping of atom positions inside an element. By introducing a single cubic cell and using linear transformations, simulations were performed by assigning degrees of freedom to the nodes of each element (instead of all atoms in the medium). The displacement vector of the atoms in the introduced elements was calculated by means of a linear mapping of 24 displacement base vectors. The method was applied to

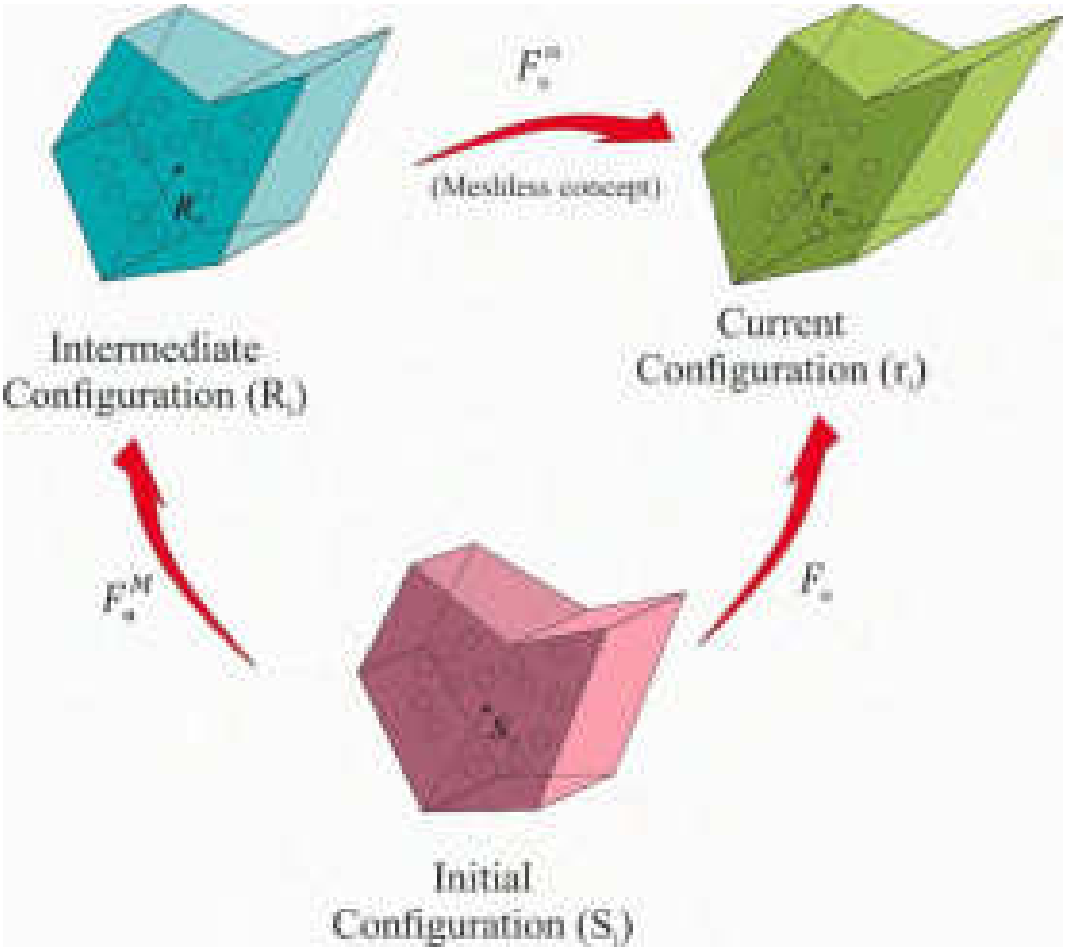

Fig. 7. Initial and deformed positions of atoms in element α.

the simulation of indentation in polyethylene by a silicone ball (Su et al., 2012) based on the experimental coefficients for friction and slip (Su et al., 2014).

Tan et al. (2008) developed an amorphous quasi-element to replace the complete atomic simulation. Moreover, Bian and Wang (2012) proposed a multiscale method to study the mechanical properties of amorphous polymers by employing the coarse-grained method for atomic regions and the finite element for the upper scale. They created a linear mapping between the two scales by defining an orientation function for atoms. Based on the Cauchy-Born rule (Ericksen, 2008), Urata and Lee proposed a multiscale method (Urata and Li, 2017) using the large-scale method introduced earlier by Parrinello and Rahman (1981). Zaccone et al. used the Helmholtz free energy and the modified Cauchy-Born rule, as introduced by Alexander based on the Taylor series expansion of the gradient field between particles up to the second order (Alexander, 1998), to calculate the shear coefficient of amorphous materials at zero Kelvin temperature (Zaccone, 2009; Zaccone and Scossa-Romano, 2011). Furthermore, hierarchal multiscale methods based on the decomposition of deformation gradient (Khoei and Jahanshahi, 2017) or correction of the stress state (Khoei et al., 2017) were developed to overcome the limitations of the Cauchy-Born rule for simulation of the hyperelastic behavior in FCC materials (Jahanshahi et al., 2020; Jahanshahi et al., 2020).

In this paper, a new concurrent multiscale method based on the maximum entropy statistical method is proposed. In addition to reducing the number of degrees of freedom and removing the frequently observed ghost forces, any irregular structure of amorphous materials can be accurately analyzed. Moreover, construction of the initial stage for generating the amorphous structure does not require any independent technique for creating a random structure. Regions with moderate conditions are discretized by the finite element method while the severe parts are simulated by the present atomistic-based multiscale technique. The corresponding finite element shape functions are computed by an entropy-based procedure. A remedy is proposed based on the mesh free techniques by constructing a continuous atomic deformation field from the imposed macro deformation gradient. The resultant deformation gradient and the stress field remain consistent in micro scales. In addition, a genetic algorithm-based method, which has less sensitivity to the choice of initial point and number of parameters, is adopted for the maximization of the entropy function. The silicon amorphous structure is considered for MD simulation in this study. It is obtained by quenching from a melted sample. The proposed concurrent multiscale method is verified and then employed to simulate an amorphous silicon specimen. Finally, the effects of sample size, strain rate, and quenching speed on rupture stress and strain in different 3D tensile simulations are investigated by the proposed multiscale method.

2. Analysis procedure

Heating a solid metal to a melting point turns it into a liquid. If the liquid is cooled down with a high temperature rate to reach a freezing point, the resultant structure of the solid material becomes glassy and amorphous. A glassy structure at a solid state has characteristics such as viscosity and irregular molecular patterns, which are similar to a liquid state. In other words, while a glassy state behaves as a solid at room temperature due to its infinite viscosity, it can still be assumed as a liquid because of its disordered, liquid–like structure of atoms and molecules. Unlike most metals, whose atoms are arranged in an ordered

Algorithm of developed multiscale method

Initialize mesh and apply the loadings and boundary conditions

Loop on the number of time steps

While Residual < tolerance

Construct the maximum entropy shape functions: $u = \sum_{i=1}^{n_n} N_i u_i$

Loop on the number of elements

Generate the tangential material stiffness of elements

Loop on the number of Gauss points

For elements in Ω_M region: $P_M = \frac{\partial W}{\partial F}$, $C_M = \frac{\partial^2 W}{\partial F^2}$

For elements in Ω_m region with atomic refinement

Estimate the coordinates of atoms: $R_i = F_M S_i$

Find the updated coordinates of atoms: $r_\alpha^h = F_\alpha^m . R_\alpha$

Smooth the deformation gradient: $F_\alpha^m = \left(\sum_1^{n_h} \omega\left(\left|\boldsymbol{R}_{\alpha\beta}\right|\right)\boldsymbol{r}_{\alpha\beta} \otimes \boldsymbol{R}_{\alpha\beta}\Omega_\beta\right)\boldsymbol{M}_{\boldsymbol{\alpha}}^{-1}$

Calculate the micro stress: $P_m = \frac{\partial \Pi_m}{\partial F} = \frac{1}{2\Omega}\sum_{i\epsilon n_t}\left(\frac{\partial \Phi}{\partial F_\alpha}\right) = \frac{1}{2\Omega}\sum_{i\epsilon n_t}\left(\frac{\partial \Phi}{\partial F_\alpha^m}\right) F_M^{-1}$

Calculate the micro modulus: $C_m = \frac{\partial^2 W}{\partial {F_\alpha}^2}$

End For

End Loop

End Loop

Assemble global stiffness matrix K: $K_{ij} = \int_{\Omega_M}\left(C_M : (\nabla N_i \otimes \nabla N_j)\right)dV$, $K_{ij} = \int_{\Omega_m}\left(C_m : (\nabla N_i \otimes \nabla N_j)\right)dV$

Compute the residual force $f = \frac{\partial \Pi}{\partial u} = \int_{\Omega_M + \Omega_m}(P_M . \nabla N)dV - \int_{\Omega_M} \rho_0 b . N\, dV - \int_{\Omega_M} t . N\, ds$

Solve $Ku - f = 0$ for displacements of nodes

End while

Update nodal displacements u_i

Postprocessing for output parameters

End Loop

Fig. 8. A brief presentation of the solution process.

crystalline pattern, amorphous alloys are non-crystalline. Conversion from liquid to solid and formation of glass occurs at a glassy temperature, where the melt cools by rapid freezing, and the viscosity steadily increases as the temperature decreases. While in crystallization, a sharp drop in volume is experienced during the cooling, no sudden change in volume is observed in the amorphous evolution and the volume and thermodynamic variables, such as entropy and enthalpy, change continuously (Elliott et al., 1983, 1983.).

One of the main mechanical properties of an amorphous metal is its limited ductility. Amorphous metals withstand only about 1 % of plastic strain, which is far less than steels and titanium alloys (Elliott et al., 1983, 1983.). In tension, amorphous metals break shortly after the

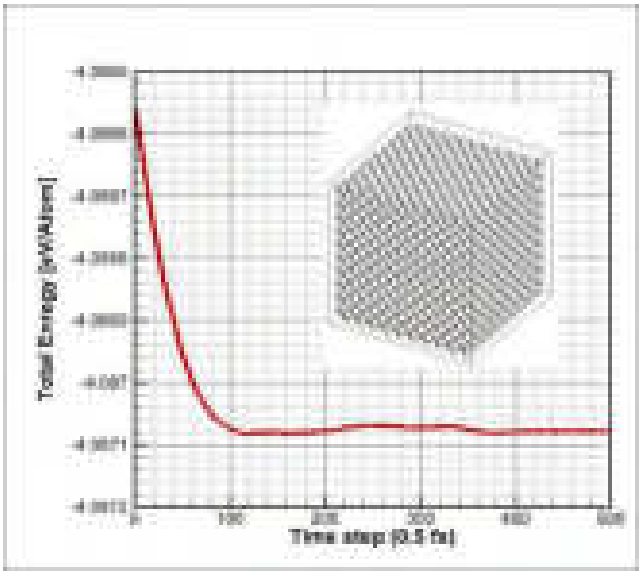

Fig. 9. Initial crystalline solid structure equilibrated at 300 K, as predicted by the MD simulation.

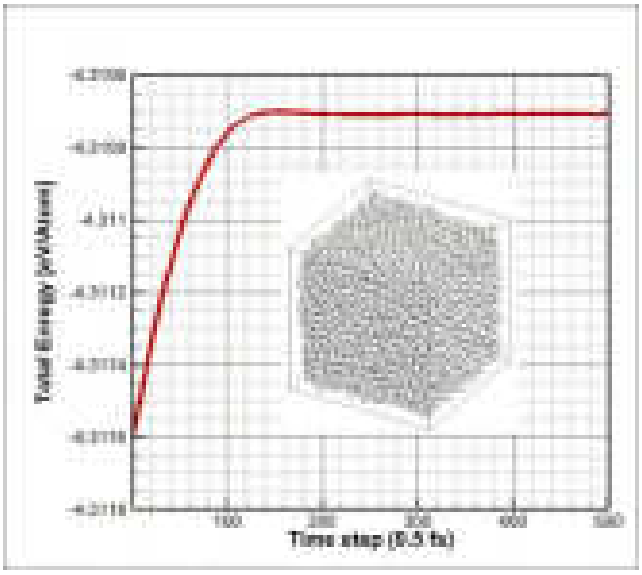

Fig. 10. Amorphous liquid structure after heating from 300 K to 3000 K, as predicted by the MD simulation.

generation of the failure mechanism without showing any major plastic deformation (Telford, 2004). Generally, the response of an amorphous material under extreme conditions is substantially influenced by atomistic and micro-scale behaviors. As a result, multiscale methods can be efficiently used to investigate the response of such complicated structures.

2.1. Multiscale model

In the present concurrent multiscale method, both macro and micro scales are considered and solved simultaneously, as schematically shown in Fig. 2. The region with severe conditions (Ω_m) is modeled by the micro/atomistic scale of the multiscale solution and the rest of the domain is simulated by the finite element method (Ω_M). One of the main ideas of the present approach is to use the maximum entropy concept in formulating the irregular structure of macro elements.

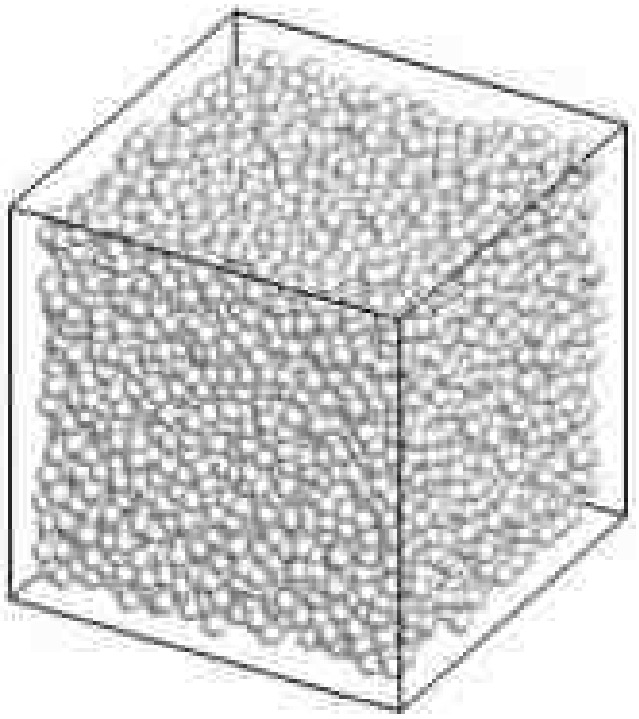

Fig. 11. Amorphous solid structure after rapid cooling from 3000 K to 300 K, as predicted by the MD simulation.

2.2. Entropy based macroscale model for irregular discretization

The amorphous domain is divided into a sufficiently fine mesh of irregular elements (see Fig. 3). Clearly, the correct choice of the dimensions of elements largely affects the simulation results. As a simple rule, it can be selected as the smallest forming and repeating chain for an amorphous polymer (Su et al., 2014; Tan et al., 2008; Bian and Wang, 2012; Urata and Li, 2017; Araújo et al., 2014; Li and Tong, 2015; Li and Urata, 2016).

The solution process for solving the model is presented by minimizing the governing energy functional Π of the system:

$$\Pi = \Pi_M + \Pi_m \tag{1}$$

where Π_M and Π_m define the macro and micro parts of the total energy.

$$\Pi_M = \int_{\Omega_M} W(F(u))dV - \int_{\Omega_M} \rho_0 b.u\ dV - \int_{\Omega_M} t_0.u\ ds \tag{2}$$

and Π_m represents the energy of the macroscale region Ω_m, as defined in section 2.4. W is the strain energy density function, $\rho_0 b$ is the body force per volume and $t_0$is the traction force imposed on the boundary and F is the deformation gradient. Nodal displacements u are approximated by the maximum entropy shape functions N_i, due to the irregular structure of elements (see Fig. 2),

$$u = \sum_{i=1}^{n_n} N_i u_i \tag{3}$$

The tensors of first Piola-Kirchhoff stress P_M and material stiffness C_M are calculated from the derivatives of W,

$$P_M = \frac{\partial W}{\partial F}, C_M = \frac{\partial^2 W}{\partial F^2} \tag{4}$$

These tensors are used to calculate the residual in the energy minimization process.

To discretize the governing equation (1), the maximum entropy shape functions N_i are used (Sukumar, 2004; Shannon, 2001).

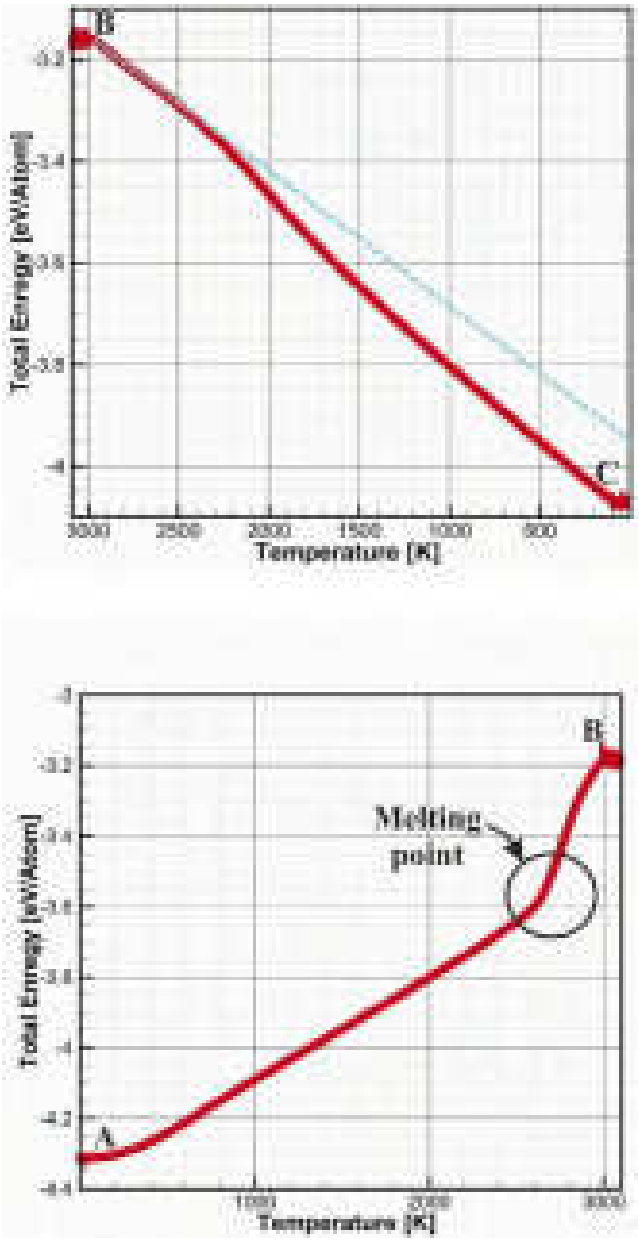

Fig. 12. Energy variations during the heating and cooling processes.

Application of the maximum entropy in macroscale problems has been extended to irregular and non-convex elements. For example, Beltzer (1996) studied the complexity of finite element using the maximum entropy method and Sukumar (2004) presented the Shannon entropy-based shape functions. Later, Arroyo and Ortiz solved a number of differential equations with the meshfree maximum entropy technique (Arroyo and Ortiz, 2006; Amiri et al., 2014; Millán et al., 2014). Moreover, Milan et al. obtained the shape functions on irregular meshes and introduced a smooth solution for differential equations using the Galerkin method (Millán et al., 2015). More recently, Norouzi et al. applied this method to solve coupled equations of porous media (Norouzi et al., 2019).

In the statistical mechanics, the entropy of a continuous distribution of the probabilistic function $p(x)$ in a system is defined as:

$$H = -k_b \int_{-\infty}^{+\infty} p(x)\log p(x)dx \tag{5}$$

where the probability function $p(x)$ of a phenomenon in a given statistical ensemble is defined by the Boltzmann coefficient, k_b. H can be regarded as a suitable criterion for evaluating the degree of certainty in the probability distribution of the ensemble. Similarly, H in a discrete set of n_e events can be rewritten as:

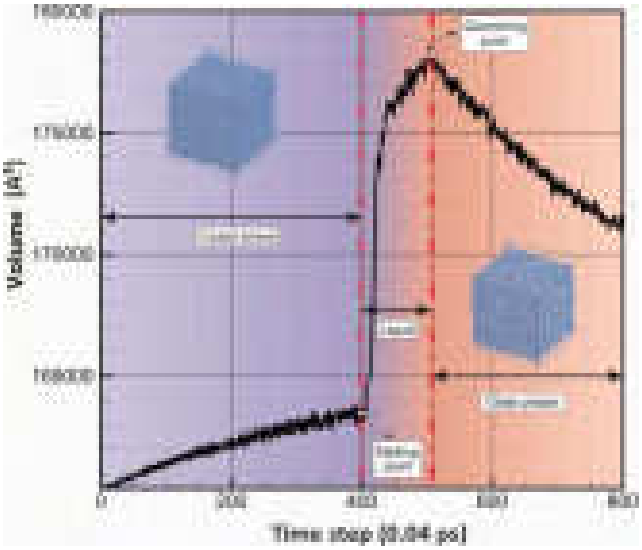

Fig. 13. Volume variations during the heating and cooling processes.

$$H = -k_b \sum_{i=1}^{n_e} p_i \log p_i \tag{6}$$

where p_i represents the probability function of the event i. It is known that in any probabilistic distribution, the sum of the probabilistic distribution functions p_i is equal to one:

$$\sum_{i=1}^{n_e} p_i = 1 \tag{7}$$

This specific characteristic can be considered as an additional constraint into the problem of entropy maximization to create function t of probabilities that best represents the system.

The probabilistic values p_i may be accompanied by nonlinear constraints χ_i, which represent the nodal coordinates x_i or y_i:

$$t = \chi - \sum_{i=1}^{n} p_i \chi_i = 0 \tag{8}$$

It should be noted that more complex constraints could be considered in the process of multidimensional problems. In general, for n_c constraints included in the maximization of function L with unknown Lagrangian coefficients λ_i, L can be written as (Sukumar, 2004; Shannon, 2001);

$$L = H(p_i) + \sum_{i=1}^{n_c} \lambda_i t_i \tag{9}$$

Now, the concept of maximum entropy can be adopted to compute the shape functions of macro elements in Ω_m by attributing the probability function of events p_i to the shape functions N_i.

The shape functions N_i for the elements are obtained by maximizing the function L_M with respect to N_i (similar to maximizing entropy of NVT or NPT ensembles in microscale),

$$L_M = H_M(N_i) + \lambda_{M1} t_{M1} + \lambda_{M2} t_{M2} \tag{10}$$

The entropy function and the constraints for obtaining the macroscale shape functions with the partition of unity property are formed as (Sukumar, 2004):

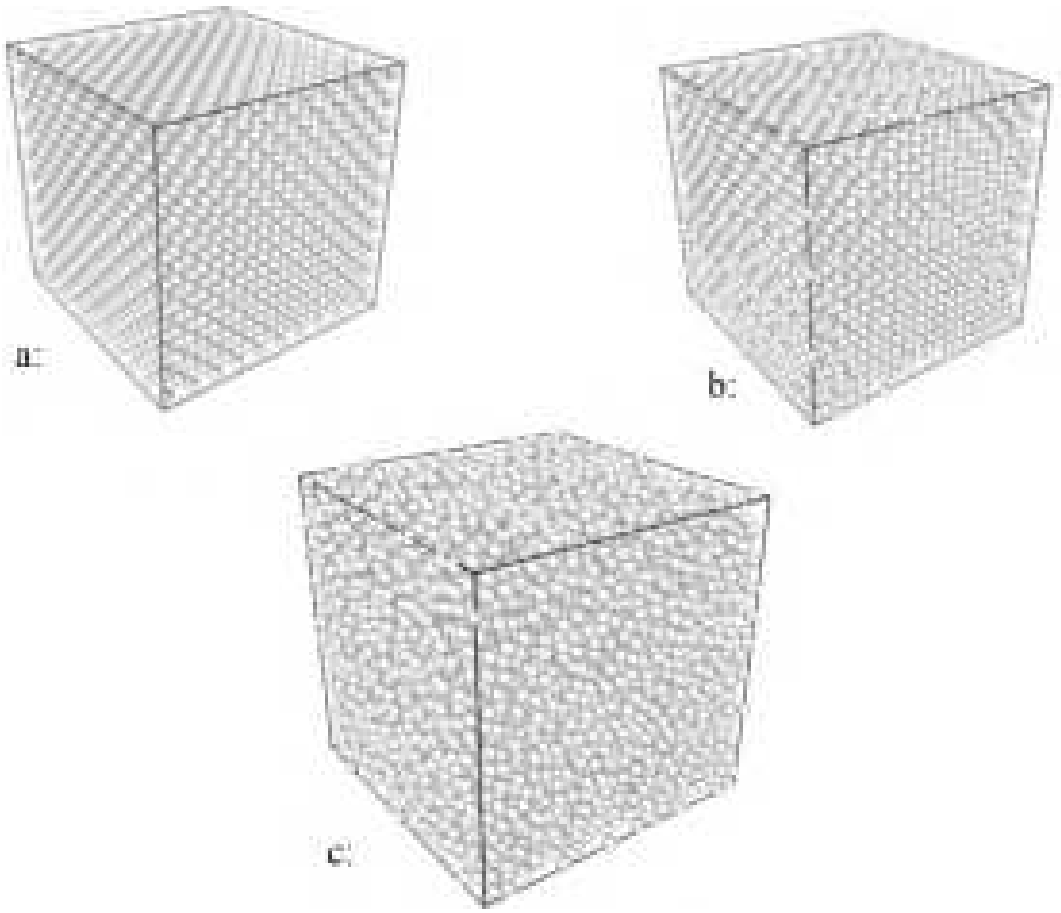

Fig. 14. Silicon atomic structures from regular to irregular states. a) Crystal b) Heated crystal at 2753 K c) Liquid.

$$H_M(N_i) = -k_b \sum_{i=1}^{n_n} N_i \log N_i \tag{11}$$

$$t_{M1} = 1 - \sum_{i=1}^{n_n} N_i \tag{12}$$

$$t_{M2} = \chi - \sum_{i=1}^{n_n} N_i \chi_i (\chi = x, y, z) \tag{13}$$

where n_n is the number of nodes in an element. The Newton-Raphson method, which depends on the initial starting point, can be adopted to maximize L_M as employed by Sukumar (Sukumar, 2004). Here, however, a genetic based evolutionary algorithm is employed for solving equation (10) to overcome the difficulties in conventional initial point dependent methods. It can readily be extended to three dimensional multiscale problems. Each chromosome is defined by four Lagrange multipliers in the binary digits and other other necessary parameters to solve this problem by the genetic algorithm are presented in Table 1.

A typical shape function contour on an irregular 2D element is illustrated in Fig. 4. More details of the approach for solving macroscale problems can be found in the reference work (Norouzi et al., 2019).

Due to the geometric requirements of irregular microstructures, concave finite elements may be required in the process of multiscale analysis. A conventional finite element procedure (mapping, interpolation and the standard Gauss quadrature) would clearly lead to the generation of negative determinant of Jacobian in some points within the element. To avoid numerical singularity and divergence, the entropy-based shape functions of irregular elements are computed in global coordinates to avoid the necessity of mapping to a parametric space and generation of non-positive Jacobian. Moreover, the well-developed sub-triangulation/subcell technique is adopted, as frequently used in XFEM, XIGA and meshless methods for integration of cracked elements/domains with concave geometries (Chin et al., 2015; Ghorashi et al., 2012; Mohammadi, 2008; Mousavi et al., 2010; Sukumar, 2013; Tabarraei and Sukumar, 2008). In this method, the integration on a concave domain is performed by the sum of integrations on a number of subcells of the domain, as schematically presented in Fig. 5. The point inside the element does not hold any degrees of freedom and only helps in dividing the element into the subcells. Moreover, it is important to note that the shape functions of all nodes of the element contribute to the computations of each integration point. The results presented in Section 4 show that the method performs well and predicts accurate results; avoiding negative Jacobian and divergence.

Integration of the function $g(x)$ on the concave domain Ω_c can be written as the sum of integrations on n_{cell} subdomains/cells (with m_G integration points each):

$$\int_{\Omega_c} g(x) d\Omega_c = \sum_{i=1}^{n_{cell}} \int_{\Omega_i} g(x) d\Omega_i = \sum_{i=1}^{n_{cell}} \sum_{k=1}^{m_G} w_{k_i} g(x_k) \tag{14}$$

where w_{k_i} is the global weighting coefficient, which corresponds to the integration point x_k in the subdomain Ω_i (Kronrod, 1965; Golub and Welsch, 1969). Moreover, new techniques such as SFEM (smoothed finite element method) (Bordas and Natarajan, 2010; Francis et al., 2017) and VEM (virtual element method) (Beirão Da Veiga et al., 2013) approaches can be applied for elements with arbitrary geometry to avoid sub-triangulation and overcome the difficulties of computing shape functions (Chakraborty et al., 2018; Natarajan et al., 2015).

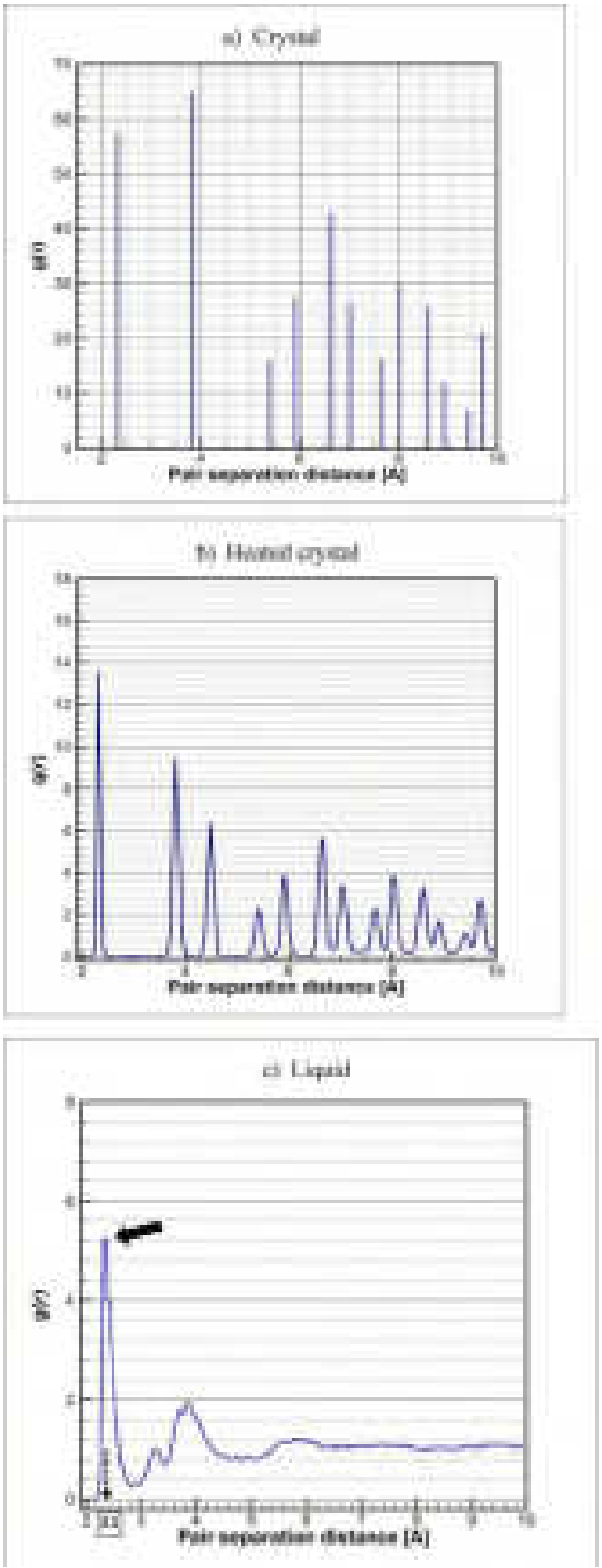

Fig. 15. Radial distribution functions associated with the 3 structures of Fig. 14.

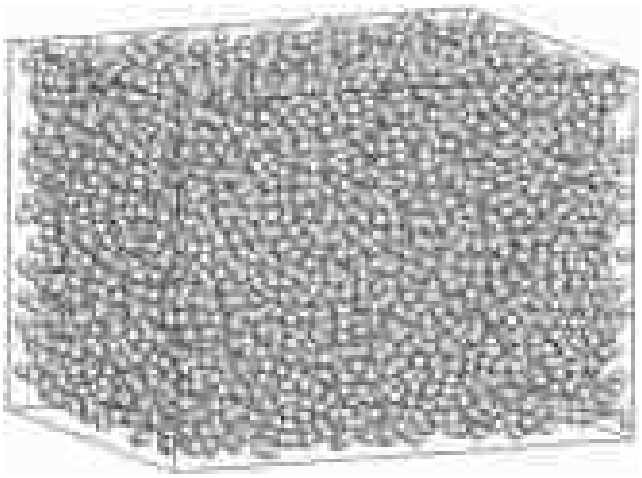

Fig. 16. MD prediction of final configuration in 0.2 strain of the amorphous specimen subjected to the unidirectional tensile stress.

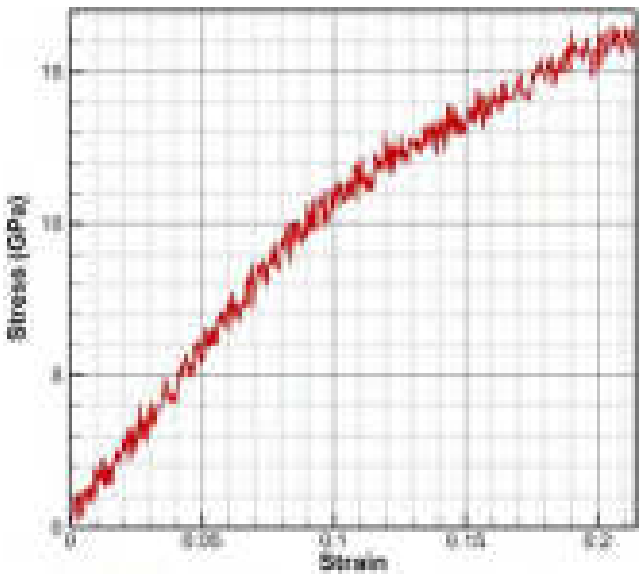

Fig. 17. Stress–strain response of the amorphous silicon in the tensile test.

2.3. Continuous deformation gradient

One of the key steps in linking the two scales in multiscale methods is the Cauchy-Born rule (Tadmor et al., 1996). Unlike crystalline materials, amorphous and polymeric materials do not follow a specific structure and therefore, the Cauchy-Born rule cannot be used directly.

Owing to the continuous nature of the finite element field, and the fact that the Cauchy-Born rule cannot be used for discrete amorphous structures directly, a continuous deformation gradient F_α on the element α is generated with the help of meshfree concepts.

Moreover, in cases where an element is positioned along a free surface (element γ in Fig. 6), its energy is not calculated correctly (due to surface effects) and unbalanced forces may be generated (Eidel and Stukowski, 2009).

Theories governing the coarse-grained methods are used to obtain a continuous deformation gradient over a single element which includes a number of discrete atoms, as depicted in Fig. 3 (similar to elements of region Ω_m in Fig. 2). The micro model is assumed to undergo a macro deformation F_α^M (Parrinello and Rahman, 1981). To avoid discontinuity in the micro deformation gradient and generation of unbalanced ghost forces, the element is first mapped to an intermediate reference

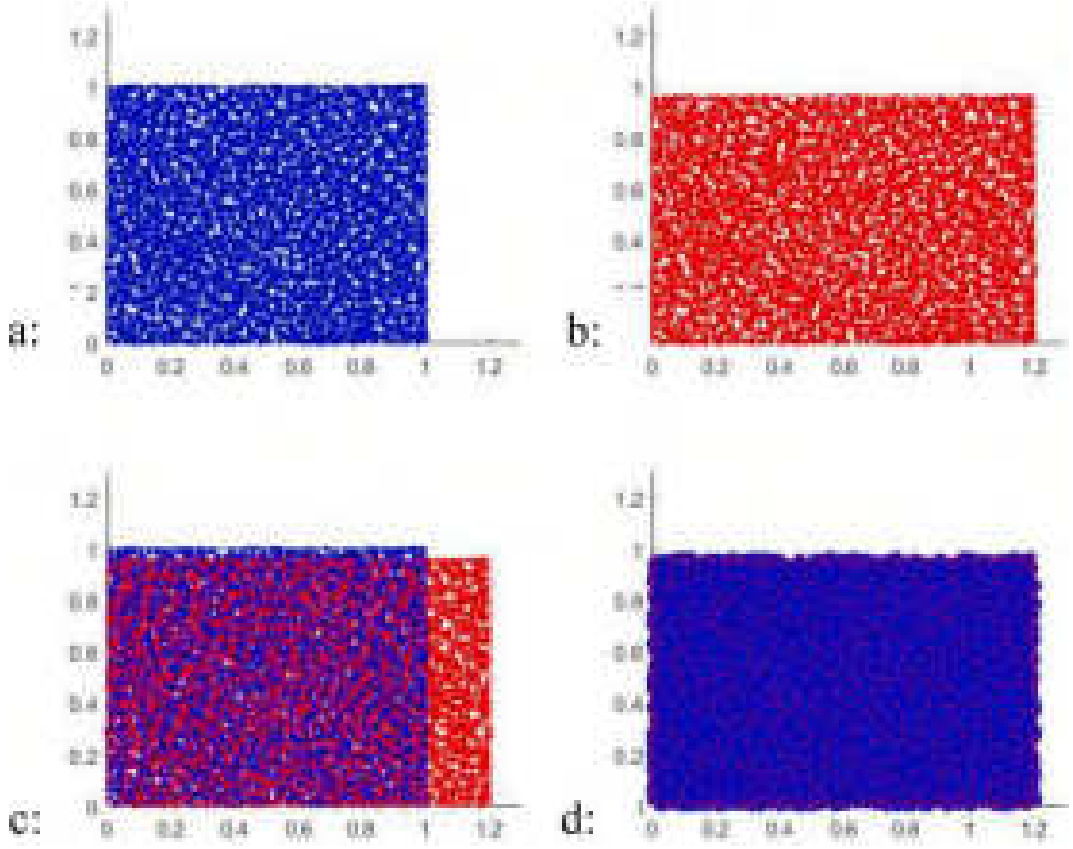

Fig. 18. Side view results of the tensile specimen.

configuration by F_α^M to determine the energy of the element correctly, as originally proposed by Parrinello for problems under extreme loading conditions (Parrinello and Rahman, 1981). In defining a continuous deformation gradient on a discrete atomic model, the micromorphic multiplicative decomposition technique (Li and Urata, 2016) is adopted to redefine the relative positions of atoms (see Fig. 7).

First, the mass center of the atoms inside the element is calculated:

$$r_\alpha(t) = \frac{1}{\sum_{i=1}^{n_\alpha} m_i} \sum_{i=1}^{n_\alpha} m_i r_i(t) \tag{15}$$

where n_α is the number of atoms inside the element α and r_i is the position of the atom i, as obtained from the MD solver. r_i can be related to the relative position $r_{\alpha i}$ of the atom i with respect to the position r_α of the center of mass:

$$r_i = r_\alpha + r_{\alpha i} \tag{16}$$

If $R_\alpha = r_\alpha(0)$ is considered to be the initial position of the mass center of element α, the relative position of this element with respect to the mass center of a neighbour element β can be defined as (Fig. 6):

$$R_{\alpha\beta} = R_\beta - R_\alpha \tag{17}$$

and for any time t,

$$r_{\alpha\beta}(t) = r_\beta(t) - r_\alpha(t) \tag{18}$$

According to Fig. 7, F_α is decomposed by the micromorphic multiplicative decomposition technique (Li and Urata, 2016). F_α contains both micro and macro deformation tensors F_α^M and F_α^m, respectively.

$$F_\alpha = F_\alpha^M F_\alpha^m \tag{19}$$

The second-order tensor F_α^m is the same macro-deformation tensor for the element which transfers the coordinates of the element to the intermediate deformation state. F_α^m is a key concept of decomposition, which defines the large-scale deformation gradient on the center of mass of each element.

Moreover, the position $r_{\alpha i}$ after deformation (solved by molecular dynamics), can be obtained by multiplying the deformation gradient F_α of the element α by the current position of the atoms $S_{\alpha i}$,

$$r_{\alpha i} = F_\alpha S_{\alpha i} \tag{20}$$

Therefore, the Cauchy-Born rule for any element can now be written as:

$$r_i = F_\alpha^m R_i \tag{21}$$

The idea of the moving least square meshfree method is now efficiently used to derive a sufficiently accurate approximation of the continuous deformation gradient field F_α^m on a discrete atomic medium. Approximating a continuous field $\Psi(r)$ can be performed by the vector of basis functions $A(r)$ and the vector of unknown coefficients c (Liu, 2009):

$$\Psi(r) = A(r).c \tag{22}$$

MLS minimization of the functional of the least square differences of the approximated field at n_a particles/atoms positioned at x_i leads to:

$$\left[\sum_{i=1}^{n_a} W(r-r_i)A(r_i)A^T(r_i)\right].c(r) - [W(r-r_1)A(r_1), \cdots, W(r-r_n)A(r_{n_a})\,].[\Psi_1, \Psi_2, \cdots, \Psi_{n_a}]^T = 0 \tag{23}$$

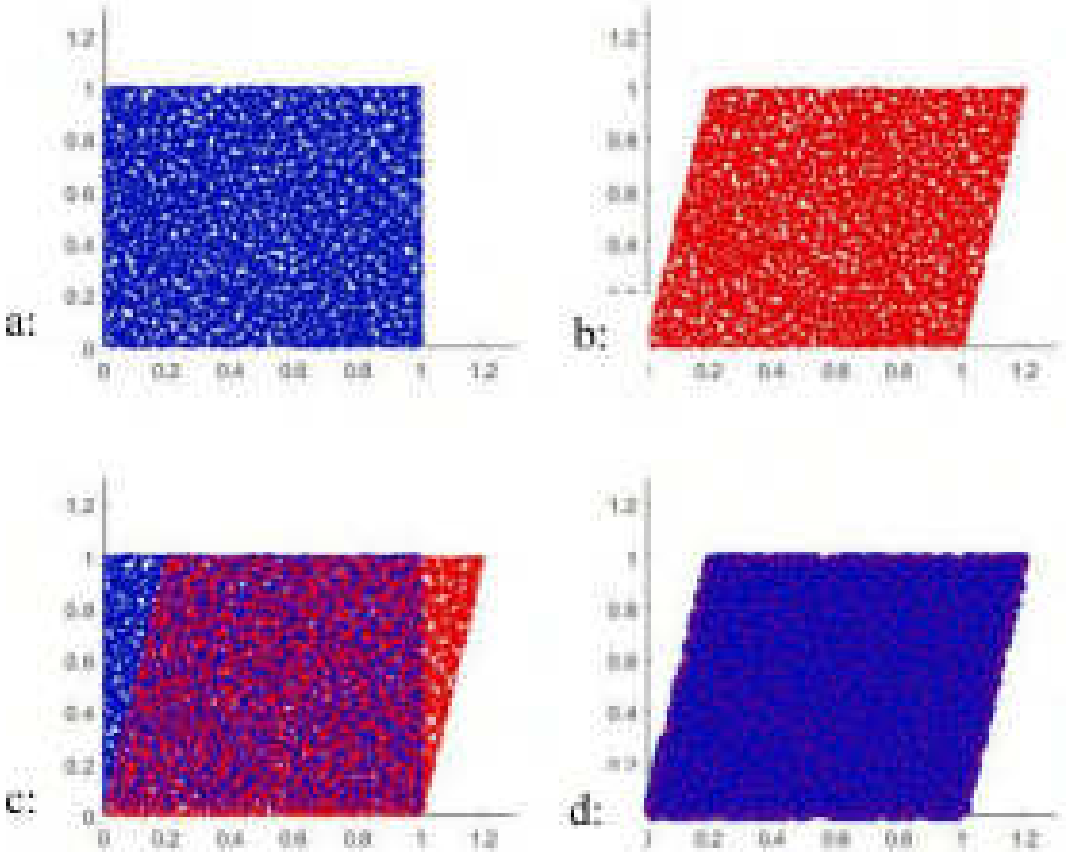

Fig. 19. Side view results of the shear specimen.

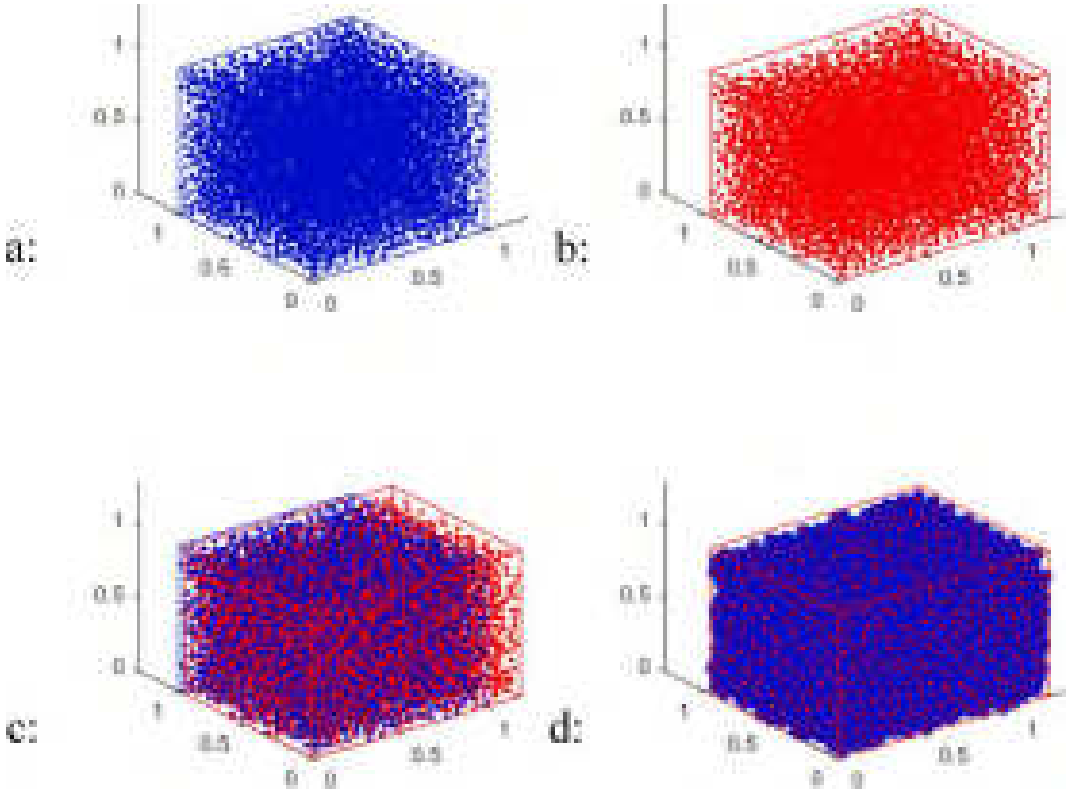

Fig. 20. Three-dimensional results of the tensile specimen.

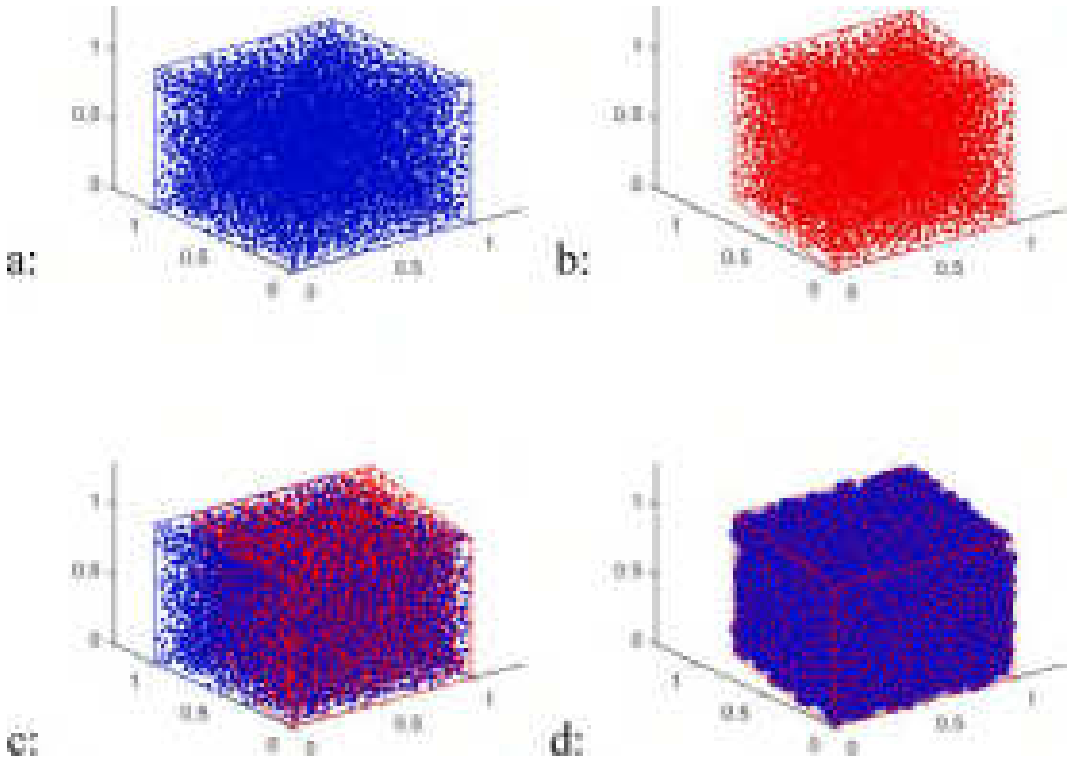

Fig. 21. Three-dimensional results of the shear specimen.

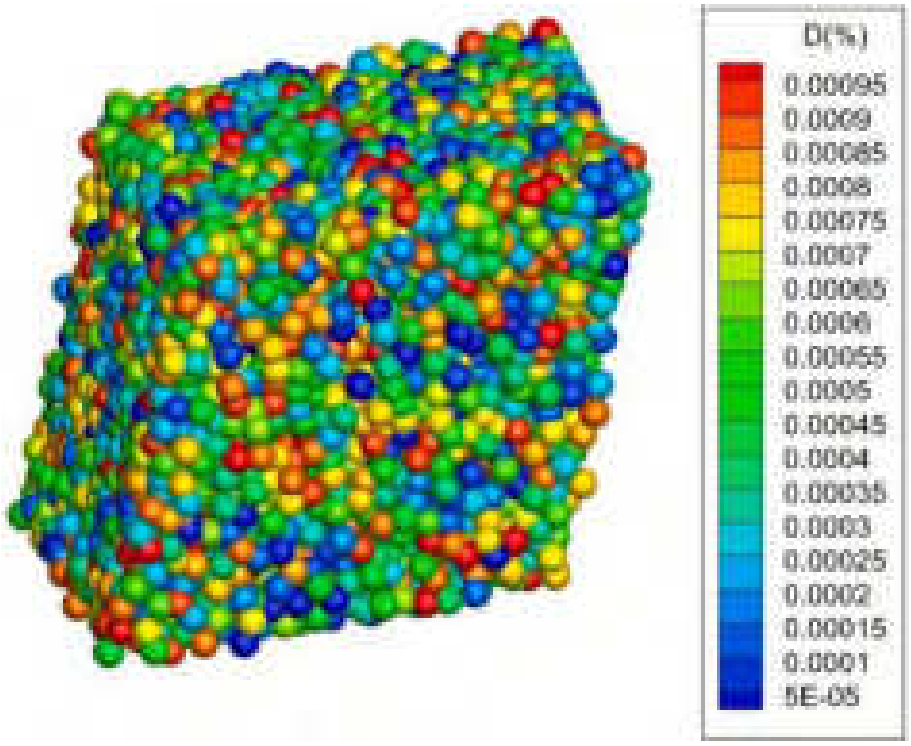

Fig. 22. Difference in atom positions resulting from the original atomic simulation and modified by the MLS method.

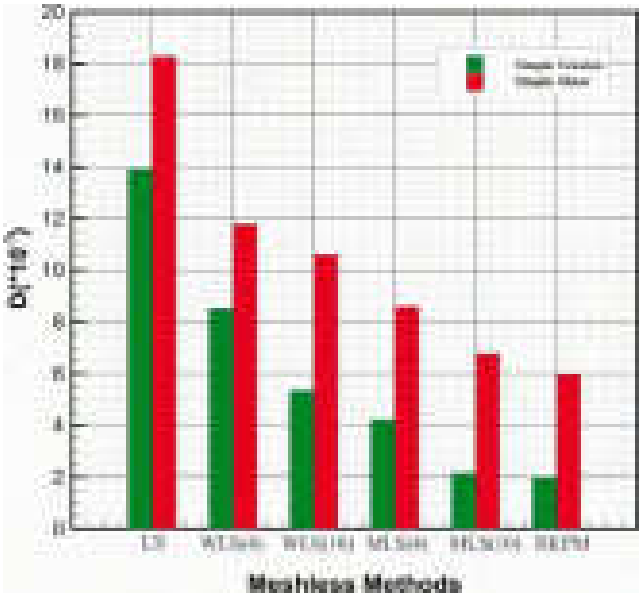

Fig. 23. Comparison of accumulative error of atoms position using different meshfree methods.

The unknown coefficients c are then obtained as:

$$c(r)=\left(\left[\sum_{i=1}^{n_a}W(r-r_i)A(r_i)A^T(r_i)\right]\right)^{-1}.[W(r-r_1)A(r_1),\cdots,W(r-r_n)A(r_{n_a})].[\Psi_1,\Psi_2,\cdots,\Psi_{n_a}]^T \tag{24}$$

where $M=\left(\left[\sum_{i=1}^{n_a}W(r-r_i)A(r_i)A^T(r_i)\right]\right)$ is the so-called momentum matrix. In the same way for a second order tensor, with the help of Ω_β (volume of element β in the same configuration state of element α) and the MLS weight function $W(|R_{\alpha\beta}|)$, it is possible to employ the meshfree technique on the tensor F_α^m of equation (21) by defining the following momentum:

$$M_\alpha=\sum_{\beta=1}^{n_h}W(|R_{\alpha\beta}|)R_{\alpha\beta}\otimes R_{\alpha\beta}\Omega_\beta \tag{25}$$

where n_h is the number of elements surrounding the element α ($\mathcal{H}_\alpha$) (see Fig. 6). Equation (25) can also be written with the help of the MLS concept, and finally:

$$F_\alpha^m\left(\sum_{\beta=1}^{n_h}W(|R_{\alpha\beta}|)r_{\alpha\beta}\otimes R_{\alpha\beta}\Omega_\beta\right)-\sum_{\beta=1}^{n_h}W(|R_{\alpha\beta}|)R_{\alpha\beta}\otimes R_{\alpha\beta}\Omega_\beta=0 \tag{26}$$

$$F_\alpha^m=\left(\sum_{\beta=1}^{n_h}W(|R_{\alpha\beta}|)r_{\alpha\beta}\otimes R_{\alpha\beta}\Omega_\beta\right)M_\alpha^{-1} \tag{27}$$

The deformation gradient associated with the initial position ($R_\alpha=r_\alpha(0)$) of an element, $F_\alpha^m(0)$, is equal to the second order unit tensor I(Li and Urata, 2016):

$$\begin{aligned}F_\alpha^m(0)&=\left(\sum_{\beta=1}^{n_h}W(|R_{\alpha\beta}|)r_{\alpha\beta}\otimes R_{\alpha\beta}\Omega_\beta\right)M_\alpha^{-1}\\&=\left(\sum_{\beta=1}^{n_h}W(|R_{\alpha\beta}|)R_{\alpha\beta}\otimes R_{\alpha\beta}\Omega_\beta\right)M_\alpha^{-1}=I\end{aligned} \tag{28}$$

It should be noted that F_α^m correlates the continuous and atomic scale configurations. In fact, without applying F_α^m in the atomic modeling, the deformation gradient cannot be applied correctly, which leads to decreased accuracy as reported in some multiscale studies (Tadmor et al., 1996) and will be discussed further in the multiscale results in Section 4.

Finally, the microscale Cauchy-Born rule can be written as,

$$r_\alpha^h=F_\alpha^m.R_\alpha \tag{29}$$

where the updated positions of atoms r_α^h are computed based on the adopted meshfree technique. The effects of a number of meshless techniques such as WLS and RKHPU[1] (Li and Liu, 1999) with different weight and basis functions are examined in the numerical simulations of Section 3.

2.4. Governing equations of the micro model

Existing forces in-between the atoms can then be obtained by calculating the energy of the micro-scale model (Li and Tong, 2015). Having known the deformation gradient F_α^m and the interatomic potential function Φ, the first Piola–Kirchhoff stress tensor P_m for element α on a gauss point can be derived from,

$$P_m=\frac{\partial\Pi_m}{\partial F_\alpha}=\frac{1}{2\Omega}\sum_{i=1}^{n_t}\left(\frac{\partial\Phi}{\partial F_\alpha}\right)=\frac{1}{2\Omega}\sum_{i=1}^{n_t}\left(\frac{\partial\Phi}{\partial F_\alpha^m}\right)F_\alpha^{M^{-1}} \tag{30}$$

Π_m is the energy function of the MD system.

$$\Pi_m=\frac{1}{2\Omega}\sum_{i=1}^{n_t}\Phi_2(r_i)+\frac{1}{2\Omega}\sum_{i=1}^{n_t}\sum_{j\neq i}^{n_t}\Phi_3(r_i,r_j,\theta_{ij}) \tag{31}$$

where Ω is the volume of macro element and n_t is the total number of atoms.

Φ is the potential function of the atomistic model, assumed to be the Stillinger-Weber (Stillinger and Weber, 1985) atomic potential in glassy metals (Hufnagel et al., 2016);

$$\Phi=\sum_{i=1}^{n_p}\Phi_2(r_i)+\sum_{i=1}^{n_p}\sum_{j\neq i}^{n_p}\Phi_3(r_i,r_j,\theta_{ij}) \tag{32}$$

$$\Phi_2(r_i)=A\left[B\left(\frac{1}{r_i}\right)^p-\left(\frac{1}{r_i}\right)^q\right]e^{\left(\frac{1}{r_i-a}\right)}$$

$$\Phi_3(r_i,r_j,\theta_{ij})=\lambda e^{\left(\frac{\gamma}{r_i-a}+\frac{\gamma}{r_j-a}\right)}\cos(\theta_{ij}+\frac{1}{3})^2$$

where n_p is the number of atoms within the MD influence domain of potential Φ.

2.5. Governing equations of the whole model

The whole energy functional of the model can be rewritten from equations (1), (2) and (31):

[1] Reproducing Kernel Hierarchical Partition of Unity.

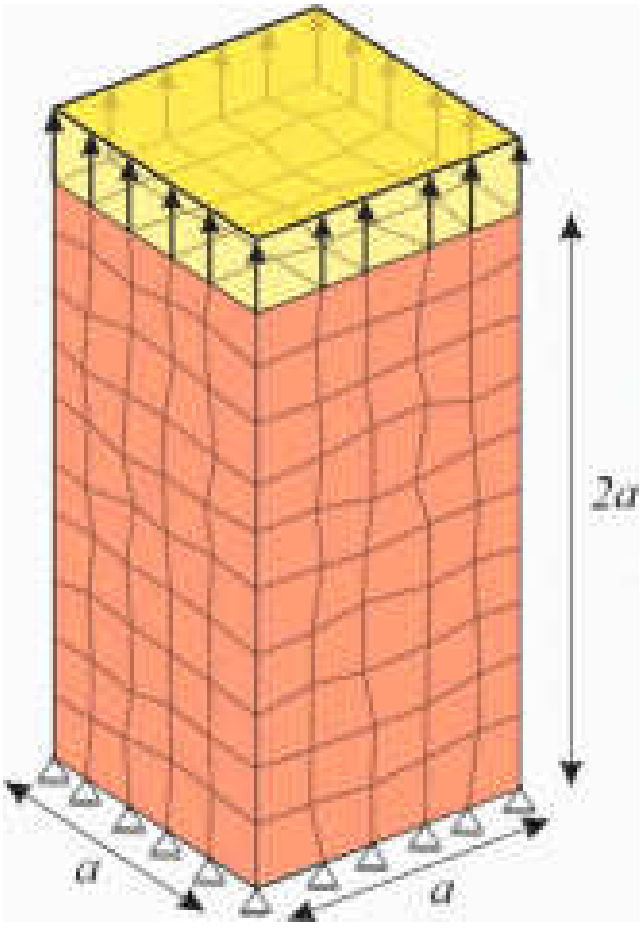

Fig. 24. Initial mesh for the multiscale modeling.

$$\Pi = \int_{\Omega_M} W(F(u))dV - \int_{\Omega_M} \rho_0 b.u\ dV - \int_{\Omega_M} t.u\ ds + \Pi_m \tag{33}$$

The micro scale first Piola–Kirchhoff stress tensor P_m is assumed to be equivalent to the macro stress ($P_M = P_m$).

The force vector can then be computed from the derivative of Π,

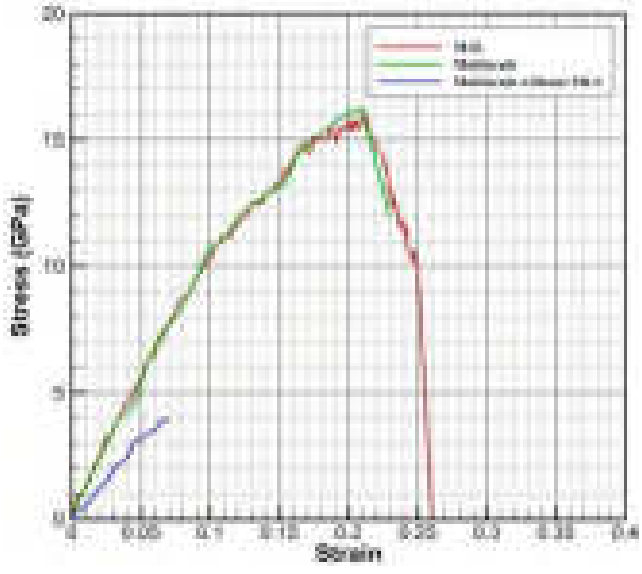

Fig. 25. Comparison of the stress–strain responses resulting from full atomic and multiscale modelings.

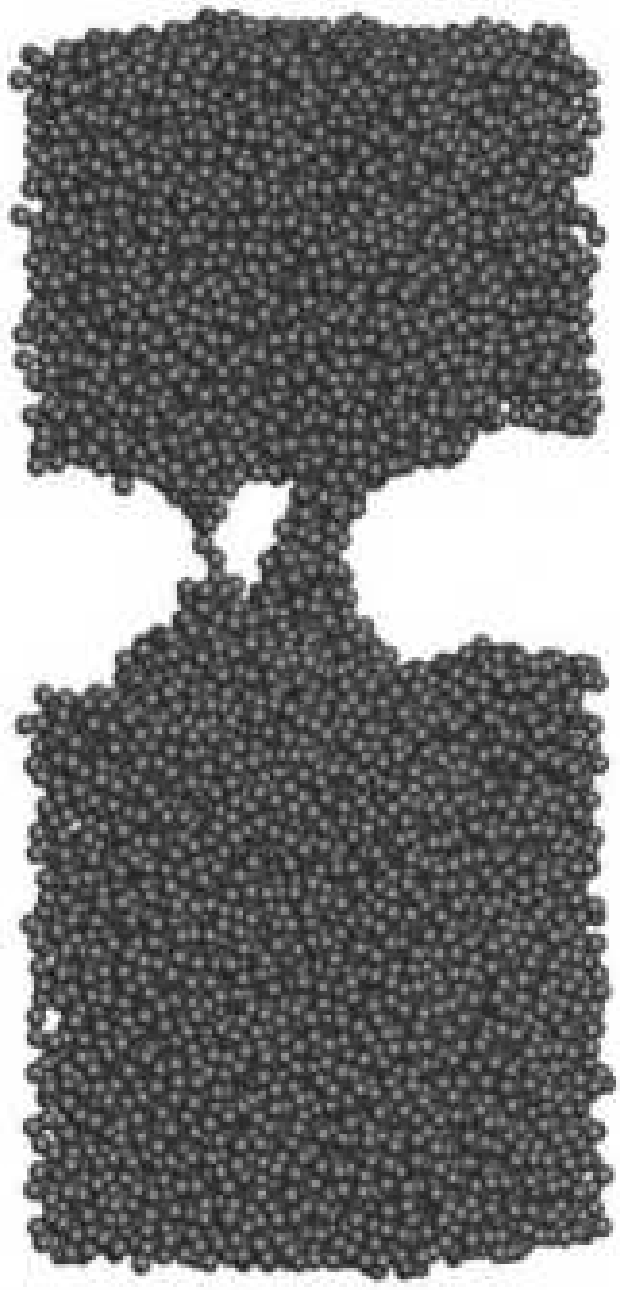

Fig. 26. Configuration of rupture in the M.D. simulation.

$$f = \frac{\partial \Pi}{\partial u} = \int_{\Omega_M} (P_m.\nabla N)dV + \int_{\Omega_M} (P_M.\nabla N)dV - \int_{\Omega_M} \rho_0 b.N\ dV - \int_{\Omega_M} t.N\ ds \tag{34}$$

The equilibrium state, in which the energy function should be at its minimum value, can be obtained by the Newton-Raphson iterative solution, as presented in the flowchart of Fig. 8. In this process, the two scales are related by the first Piola–Kirchhoff stress P_m from the micro-scale according to equation (34), in which the equilibrium state is obtained.

3. MD simulations

Principles, formulations, algorithms and the necessary concepts were discussed in previous sections. In this section, the results of performed simulations are presented and discussed. The predicted characteristics

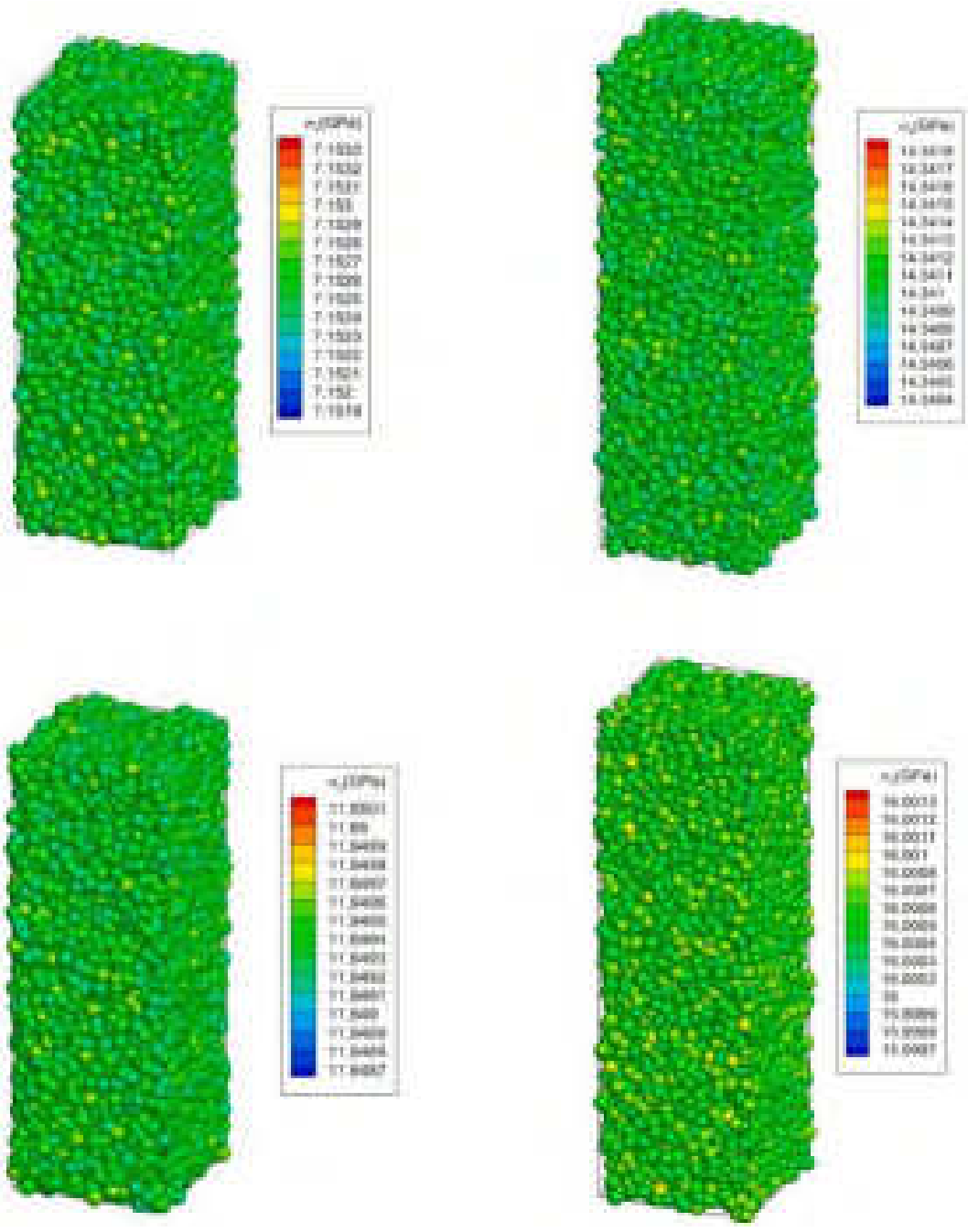

Fig. 27. Stress distribution on atoms in different loading steps (6.44%,12.38%, 16.21% and 19.98% strains), predicted by the proposed multiscale approach.

and behavior of amorphous material are compared with references to validate the proposed multiscale procedure. Simulations are performed by employing the open-source LAMMPS software for MD simulations and the home-developed multiscale solutions.

3.1. Generating the irregular microstructure with MD

In the following, the amorphous silicon is selected for simulation because of its atomic composition and simplicity. First, by heating this material to the melting point, it becomes a liquid. Then, it turns into an amorphous structure by cooling. While a regular crystalline structure is considered for silicon before melting, an irregular structure is obtained. Also, the interatomic potential of Stillinger-Weber which consists of two-body Φ_2 and three-body Φ_3 interaction terms is used (Stillinger and Weber, 1985). The parameters of this potential are defined as:

$$\begin{aligned} &A = 7.049556,\ B = 0.6022245584 \\ &\lambda = 21.0,\ \gamma = 1.2,\ p = 6,\ q = 0,\ a = 1.8 \end{aligned} \tag{35}$$

For the motion equations, the Verlet velocity algorithm is adopted for updating the positions of particles and the Nose-Hoover thermostat is employed for controlling the temperature. Further details will be explained in each step.

First, the crystalline silicon (with the size of $54 \times 54 \times 54A^3$) is modeled by 8000 atoms, as shown in Fig. 9. The model is equilibrated at an initial temperature of 300 K, with a time step of 0.5 fs using an NPT ensemble at an atmospheric pressure. The equilibrium time of the system should be selected in a way that ensures the system is fully balanced and its energy remains at the lowest level, as depicted in Figs. 9 and 10.

After the system reaches equilibrium, the temperature is increased to 3000 K to reach the melting point (with NPT ensemble). For each

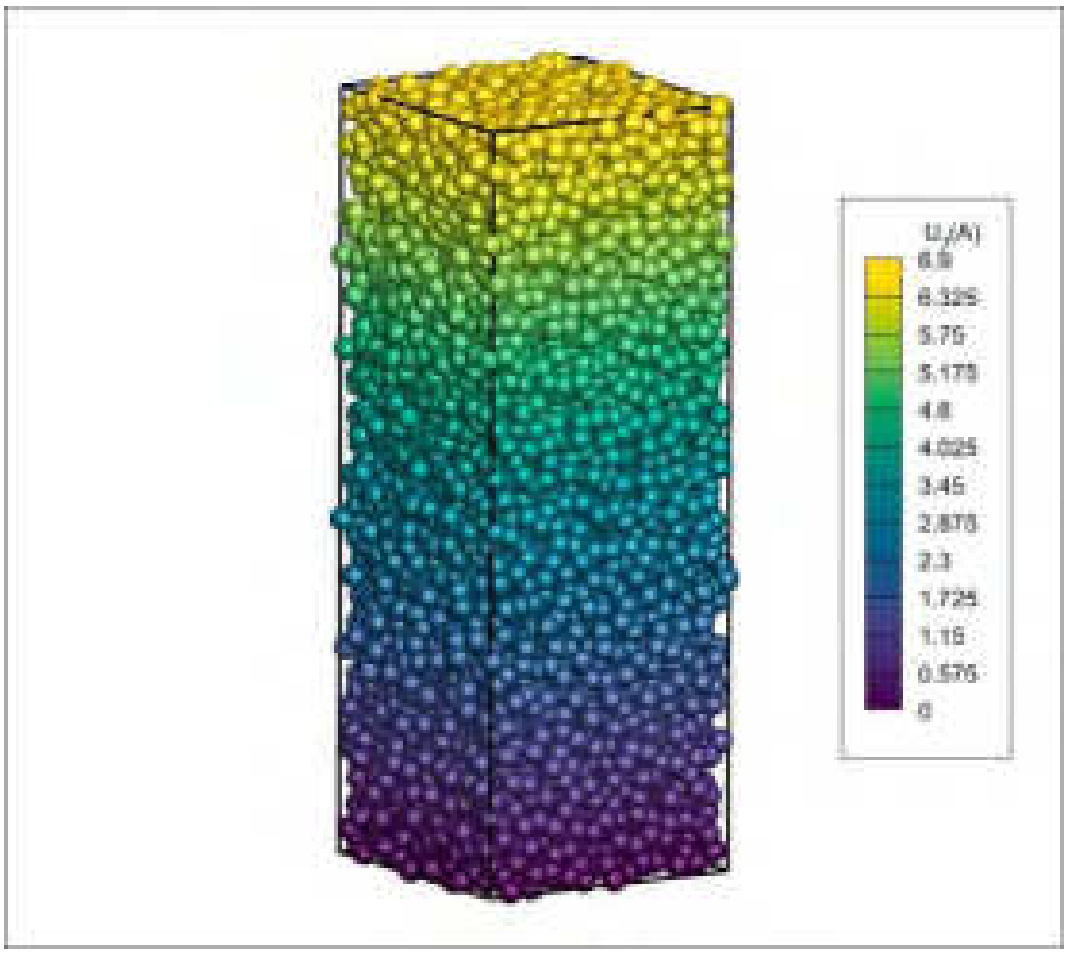

Fig. 28. Displacement contour on atoms (at 6.44% strain), predicted by the proposed multiscale method.

temperature step (1 K), the system is relaxed at 2 ps so that the transition of the system from solid to liquid takes place (as shown in Fig. 10).

The liquid obtained from the melting of crystalline solid is then cooled by a rapid cooling rate (1 K / ps in an NPT ensemble is used in this simulation). Fig. 11 clearly shows that the solid obtained at 300 K has an amorphous structure. Fig. 12 illustrates the energy variation during this process with clear jumps of energy associated with the changes of material state from solid to liquid and vice versa. It is observed that turning from crystalline to an amorphous structure is characterized by a sharper jump.

The sample volume increases due to melting and its structure is converted to an amorph, as depicted in Fig. 13. It is observed that the volume of the sample shows a dramatic increase during the heating, leading to a 10 % decrease in density, as reported in (Glazov and Shchelikov, 2000).

After further heating, the volume decreases but does not reach the initial value. As a result, the density of amorphous material remains lower than its regular structure at the same temperature, which is in complete agreement with the data obtained from computational simulations and experimental tests in the literature (Elliott et al., 1983; Sasaki et al., 1994; Glazov and Shchelikov, 2000; Logan and Bond, 1959).

3.2. Micro-scale properties

Micro-scale properties, such as the radial distribution function, which indicates how the density is distributed in the body, are important in numerical simulations (Ojovan and Louzguine-Luzgin, 2020). The radial distribution function of a set of particles, denoted by $g(r)$, indicates the probability of finding a pair of particles with a distance r from each other. This function somehow illustrates the local structure and adjacency of the atoms to each other. For a homogenous set of n_t particles in volume V (density ρ), the radial distribution function is defined by:

$$g(r) = \frac{2}{\rho n} < \sum_{i}^{n_t} \sum_{j \neq i}^{n_t} \delta(r - r_{ij}) dr > \tag{36}$$

where <> represents the averaging over time and r_{ij} is the distance between atoms i and j.

The radial distribution function depends on the temperature and density of the system (Kim and Medvedev, 2006). It can be indirectly used to represent the phase of a system on the edge of the solid–liquid state. The radial distribution function for the crystalline structures at a temperature below the melting point is a series of Dirac-delta functions that represent the crystalline structure. After the melting temperature, this function is transformed into Gaussian functions due to thermal irregularities. These delta or Gaussian functions may well represent the local density changes in atomic structures.

The radial distribution function in the melting process for three atomic structures of silicon (Fig. 14) is plotted in Fig. 15. It is observed that the radial distance distribution changes from the regular to the irregular structure at around 2.5 and the distributions are as reported in (France-Lanord et al., 2014; Kugler et al., 1993).

3.3. Mechanical properties

After examining the micromechanical properties, now the

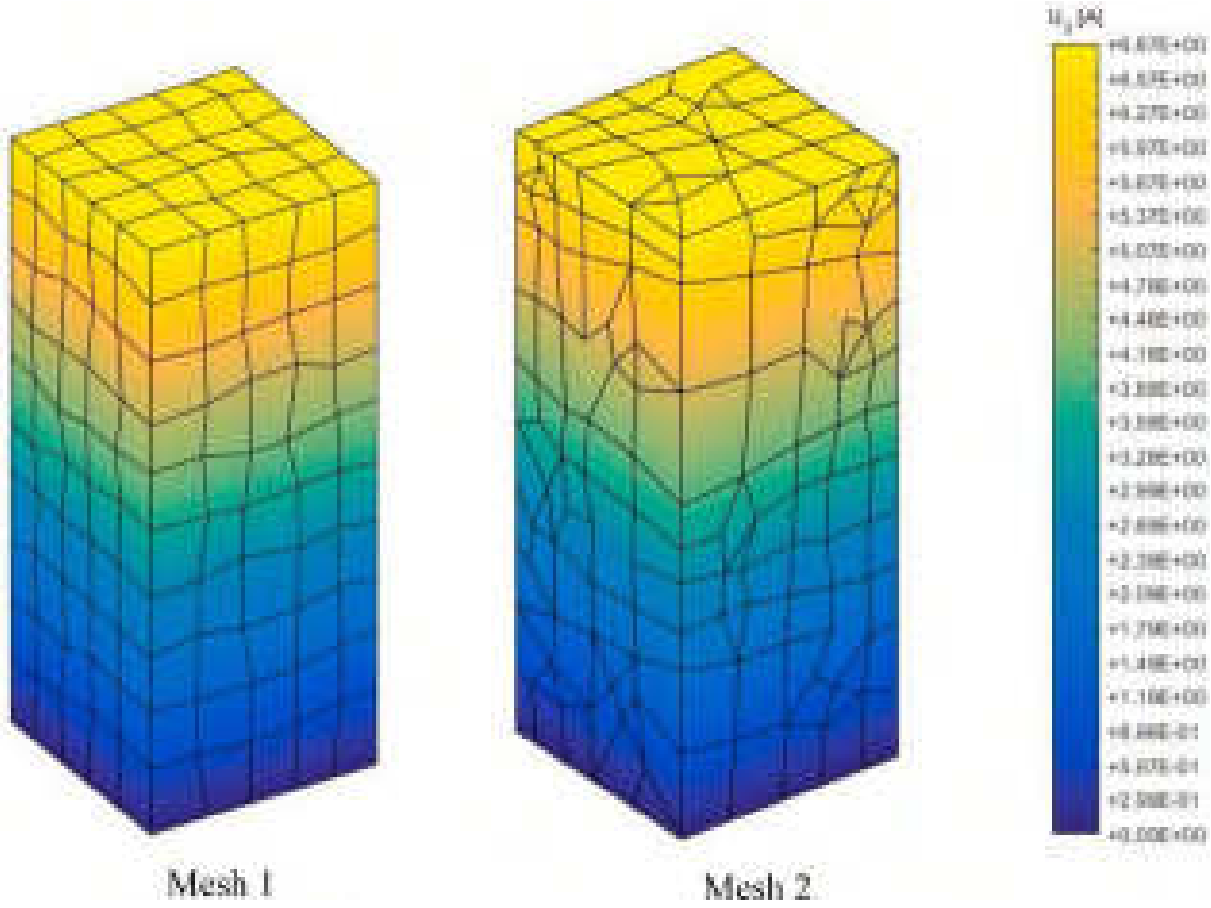

Fig. 29. Deformation contour in the longitudinal direction in two different macroscale meshes.

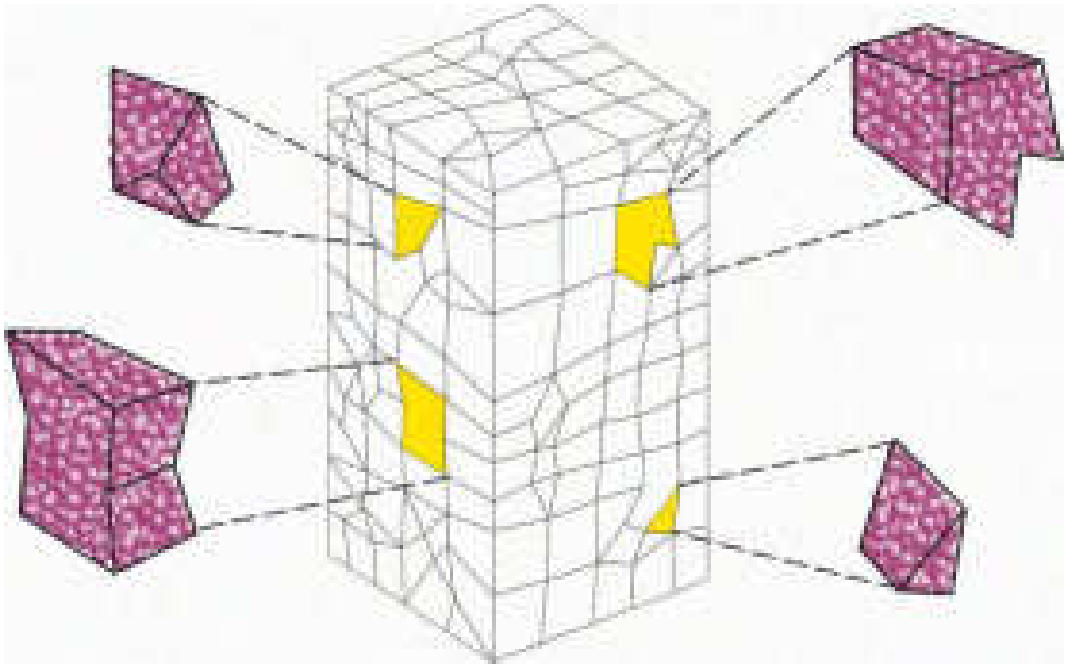

Fig. 30. Typical irregular elements at the initial configuration with the a different number of nodes.

mechanical properties are studied. The obtained amorphous specimen (configuration of Fig. 11) is loaded at a constant rate of unidirectional tensile stress. The final configuration is illustrated in Fig. 16.

The stress–strain diagram of the amorphous silicon with 8000 atoms in the tensile test simulation (with the NVT ensemble) is shown in Fig. 17. The canonical ensemble with a time step of 0.5 fs is chosen to

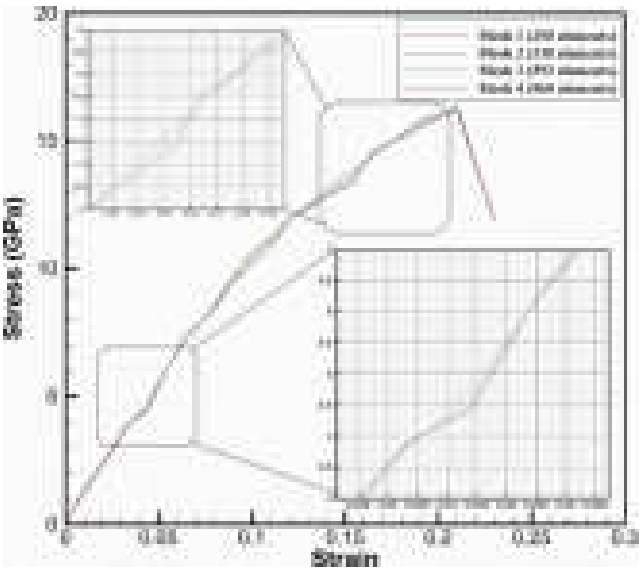

Fig. 31. Stress–strain for multiscale simulations with different meshes.

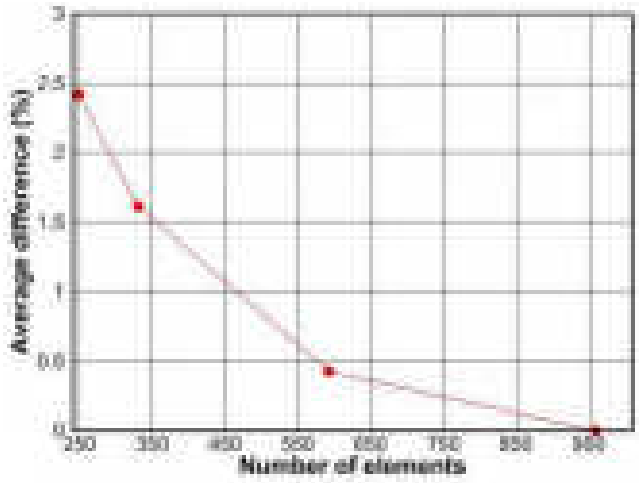

Fig. 32. Average difference in stresses for four different meshes.

capture the brittle behavior of the sample, as used in the literature for glassy materials (Jia et al., 2016; Muralidharan et al., 2005; Pedone et al., 2006; Pedone et al., 2008). The Young's modulus, determined by calculating the slope of the stress–strain diagram in the linear region, is obtained 108.3 GPa, which is similar to the values reported in the literature (Freund and Suresh, 2004; Jing and Meng, 2010; Shodja et al., 2014; Yuan and Huang, 2012).

3.4. Continuous deformation gradient

After generating the amorphous irregular structure, as described in Section 3.1, the results of obtaining a continuous deformation gradient field are presented. The initial and final geometric positions of the atoms in the sample are presented in Figs. 18-21.

In these Figures, subfigures depict the initial position (a), the final deformed configuration of MD simulation (b), and the result of atomic simulation in both initial and final states of meshfree technique (c), and a comparison of both results of atomic simulation (red atoms) and the proposed method (blue atoms) (d). Since, the illustrations show overlapped atoms due to their finite size representation, a better overview in terms of the relative difference of the two methods is represented in

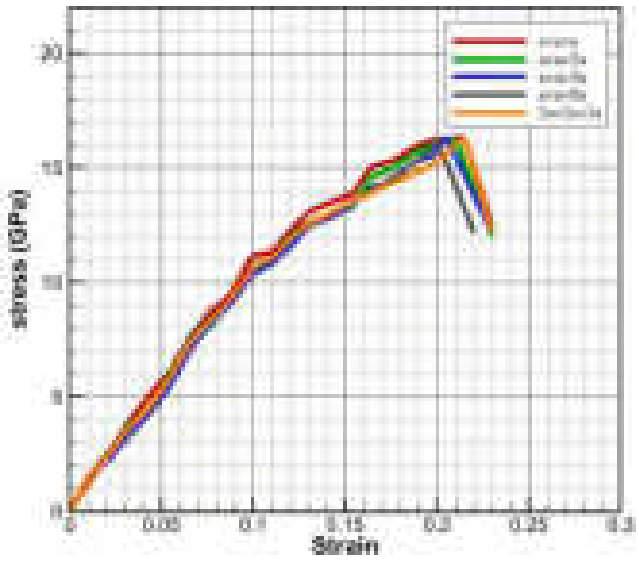

Fig. 33. Effect of sample size on the stress–strain response for the tensile test.

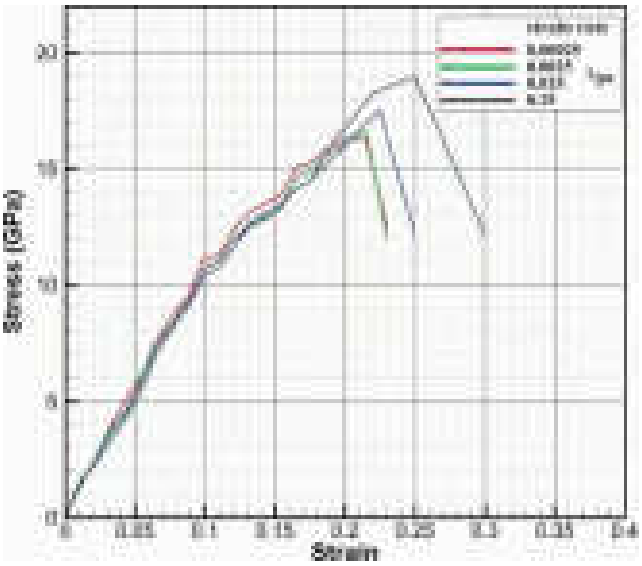

Fig. 34. Effect of strain rate in the tensile test.

Fig. 22.

The accumulative difference for n atoms of the specimen, as defined by equation (37), for the shear deformation simulation is about 2.5×10^{-3}. Fig. 23 compares the accumulative difference (37) predicted by different meshless techniques in a negative logarithmic scale. The meshless techniques include the least square method (LS), weighted least square techniques (WLS) with 4 and 10 terms of basis function, MLS with 4 and 10 terms of basis functions, and the reproducing kernel particle method (RKPM).

$$D = \sum_{i}^{n_t} \left| \frac{(r_i - \bar{r}_i)}{r_i} \right| \tag{37}$$

4. Multiscale simulation

In this section, the results of the multiscale simulations are presented. Fig. 24 illustrates the initial mesh corresponding to the irregular amorphous structure after the cooling process. It consists of 16,000 atoms and 250 unstructured elements with eight Gauss points each. It

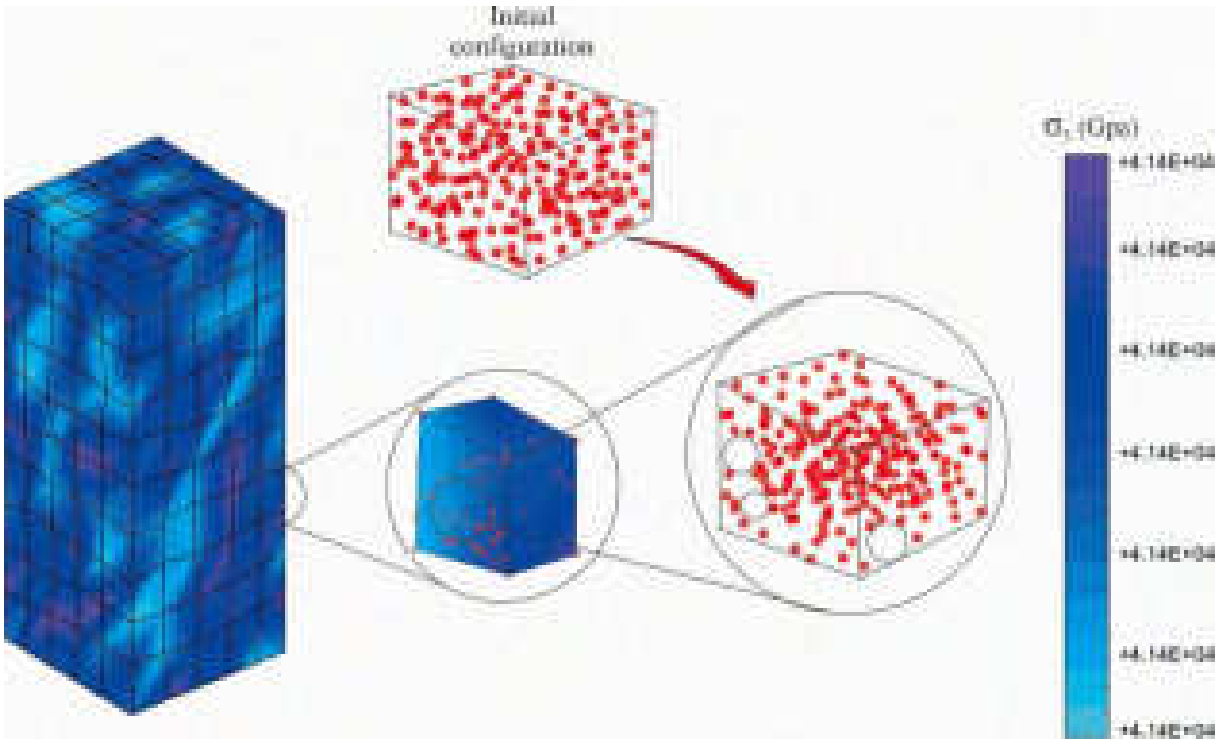

Fig. 35. Creation of nanovoids as predicted by the multiscale simulation of the tensile test (3.83% strain).

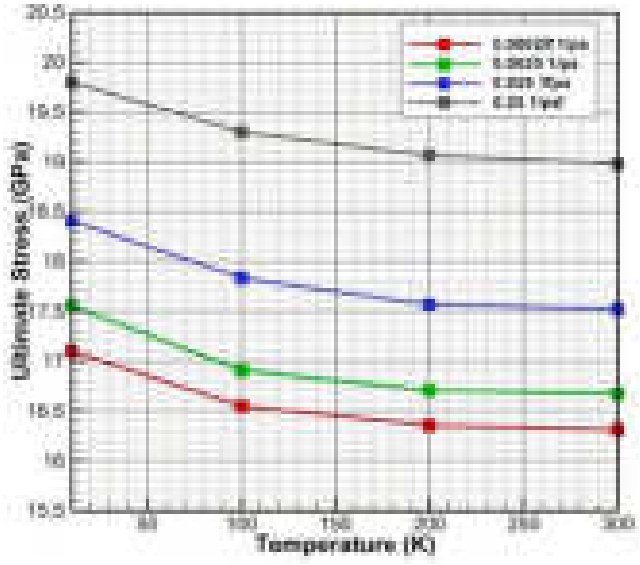

Fig. 36. Effect of solid state temperature on the rupture stress.

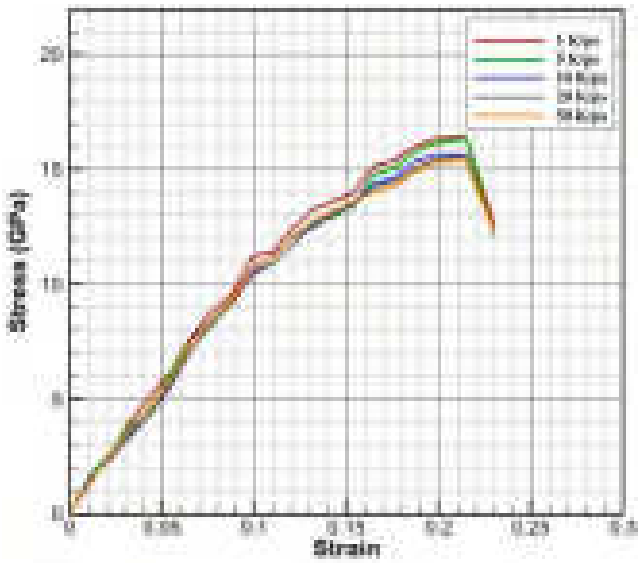

Fig. 37. Results of the effect of quenching speed on the stress–strain response of the tensile test.

should be noted that due to the irregular destitution of atoms in the specimen, each element has a different number of atoms. Shape functions attributed to unstructured meshes are computed by the maximum entropy solution, based on parameters presented in Table 1.

The predicted stress–strain diagram is plotted in Fig. 25 for 4528 number of steps, which compares the present multiscale results with the solution obtained by full MD simulation. Moreover, the multiscale simulation is performed without the meshless-based refinement of the deformation gradient, which quickly diverges and terminates in the initial steps, a clear indication of the necessity of the modified deformation gradient for analysis of the amorphous materials.

It should be noted that the final stage of the multiscale simulation associated with the strain of 0.22, can be related to the onset of failure, as observed in Fig. 26 for MD simulation.

Fig. 27 shows the stress distribution on the atoms of the sample in different loading steps, which are expectedly uniform due to the unidirectional tensile nature of the test. The corresponding displacement contour at the final step of 0.06 strain is plotted in Fig. 28. The simulation runtime, on a 2.6 GHz-Intel Xeon E52690 consisting 56-core CPU is 18.3 and 3.2 min for full molecular dynamics and multiscale analyses, respectively.

Moreover, the displacement contour can be illustrated on the macro elements, as depicted in Fig. 29 for two totally different possible meshes. Typically, various elements include approximately 70 atoms and consist

of 5, 6, 8, 10 and 12 nodes, as depicted in Fig. 30. Both displacement distributions are uniform.

The stress–strain responses of these two meshes are illustrated in Fig. 31, which shows very similar trends. Furthermore, in order to examine the accuracy of the adopted sub-cells technique for the integration of the concave finite elements (Mesh 2), a fine mesh consisting of convex elements (Mesh 3) is analyzed. Mesh 3 matches the same geometry of sub-cell technique of Mesh 2 but with additional inside nodes and independent degrees of freedom. Again, a very good agreement is observed, illustrating the accuracy of the adopted technique for concave elements.

In order to assess the discretization error of the present simulations, four different meshes with 250, 330, 593, and 960 elements (at the macro scale) are employed. Fig. 32 shows the average difference (defined in Eq. (38)) of the stress results in n_p number of data points. Clearly, a converged solution is demonstrated.

$$\frac{Average\ of}{difference} = \sum_{i=1}^{n_p} \frac{1}{n_p} \left| \frac{\left(\sigma_i^{coarse} - \sigma_i^{fine}\right)}{\sigma_i^{fine}} \right| \times 100 \tag{38}$$

After validating the developed procedure with the results of an all-atomic sample presented in the previous section, the effects of sample dimensions, quenching speed and loading rate on the results of the tensile test are investigated.

First, the effect of sample dimensions is examined. The reference sample is assigned with dimensions $a \times a \times a$ and the rest are scaled in different directions. Each number represents the scaled coefficient compared with the reference sample. For example, the sample $a \times a \times 2a$ defines a sample with twice the dimension of the reference sample in the third direction (which now consists of 500 elements). Note that all specimens are tested for traction along the third direction.

The results, presented in Fig. 33, clearly show that the change in the size of the sample has no effect on the final rupture stress. There is a small decrease in the rupture strain for larger sizes, which can be due to the increase in the distribution of surface defects in larger specimens (Pedone et al., 2008; Yuan and Huang, 2012; Zhou et al., 2015).

The strain rate is another important factor that expectedly affects the stress–strain response of the tensile sample. According to Fig. 34, the sample is tested at four different strain rates and the results of multiscale modeling are presented. It is observed that, at high strain rates, the sample breaks at higher stresses and strains, which may be due to the lack of sufficient time in connection of the nanovoids created during the deformation. The nanovoids can be typically tracked, as illustrated in Fig. 35. It is also noted that the two lower tensile rates show relatively similar behavior, indicating that the strain rate is practically ineffective below a certain value.

So far, all simulations have been carried out at a constant temperature (300 K). Now, in addition to the strain rate, the effect of temperature is examined, as depicted in Fig. 36, which shows that the final rupture stress is affected and decreased by increasing the temperature of the solid state of the sample. Due to high atomic motions and vibrations in higher temperatures, the occurrence of initial defects in atomic bonds facilitates the rupture to occur faster (Chang and Fang, 2003; Vu-Bac et al., 2015; Zhao et al., 2015).

Finally, the effect of quenching speed on this simulation is studied. As mentioned before, an amorphous sample uses a fast-cooling process in which the quenching rate may become important. According to Fig. 37, while the quenching velocity has a little effect on the rupture strain, it does influence the level of rupture stress. The reason can be attributed to the micromechanical properties of the material. The faster the quenching rate, the more the material retains its liquid structure and the more initial defects remain, which leads to lower resistance of the sample (Jana et al., 2019; Wang et al., 2009; Sanchez et al., 1984).

5. Conclusions

Multiscale analysis of disordered materials such as amorphous specimen is numerically addressed by the maximum entropy statistical method combined with a meshless-based continuous deformation gradient field over the discontinuous atomic model. The developed method is categorized as a novel concurrent multiscale method, where both scales are simultaneously solved by the concept of maximum entropy. Exciting multiscale studies have either used regular elements with coarse-grained methods or have dealt with the atomic and F.E. discontinuous regions. In this study, a meshless remedy for constructing a continuous deformation gradient is employed to overcome these difficulties. The ideas of meshfree methods are used to derive an accurate continuous form of the deformation gradient field on a discrete atomic medium. Moreover, a genetic algorithm-based approach is adopted for the maximization of the entropy functions to overcome the sensitivity of the solution to the choice of initial point and number of parameters.

A regular crystalline structure is considered for silicon, followed by melting and rapid quenching to obtain an irregular structure. Density jump, radial distribution function and other mechanical properties are obtained, which are in good agreement with the literature. Furthermore, the multiscale solutions for the displacement and stress contours are compared with the results obtained from the full molecular dynamic simulation, showing a very close agreement.

It is observed that the sample size has practically no effect on the final rupture stress, However, the rupture strain slightly decreases because of the distribution of surface defects in larger specimens. Furthermore, the effect of strain rate is investigated for a range of practical rates and the results illustrate that due to the lack of sufficient time for nanovoids to connect in high strain rates, the sample breaks at substantially higher stresses and strains. Moreover, the effect of solid-state temperature on the ultimate rupture stress is investigated, where the higher temperature leads to less resistance of the sample. Finally, it is shown that the quenching velocity has a significant effect on reducing the rupture stress due to the micromechanical properties of the material.

The methodology of this work has prepared the groundwork for further investigations on the response of other more complicated amorphous materials. Future investigations may lead to a better understanding of the complex behavior of amorphous molecular structures under thermal loadings.

Declaration of Competing Interest

The authors declare that they have no known competing financial interests or personal relationships that could have appeared to influence the work reported in this paper.

Data availability

The authors are unable or have chosen not to specify which data has been used.

Acknowledgements

The authors gratefully acknowledge the High-Performance Computing Laboratory (HPC Lab), University of Tehran for the technical support. The financial support of Iran National Science Foundation (INSF) is gratefully acknowledged (Grant No. 96013175).

References

Abdolhosseini Qomi, M.J., Krakowiak, K.J., Bauchy, M., Stewart, K.L., Shahsavari, R., Jagannathan, D., Brommer, D.B., Baronnet, A., Buehler, M.J., Yip, S., Ulm, F.J., Van Vliet, K.J., Pellenq, R.J., 2014. Combinatorial molecular optimization of cement hydrates. Nat. Commun. 5, 4960.

Alexander, S., 1998. Amorphous solids: their structure, lattice dynamics and elasticity. Phys. Rep. 296 (2–4), 65–236.

Alizadeh, O., Eshlaghi, G.T., Mohammadi, S., 2016. Nanoindentation simulation of coated aluminum thin film using quasicontinuum method. Comput. Mater. Sci. 111, 12–22.
Alizadeh, O., Mohammadi, S., 2019. The variable node multiscale approach: coupling the atomistic and continuum scales. Comput. Mater. Sci. 160, 256–274.
Amiri, F., Anitescu, C., Arroyo, M., Bordas, S.P.A., Rabczuk, T., 2014. XLME interpolants, a seamless bridge between XFEM and enriched meshless methods. Comput. Mech. 53 (1), 45–57.
Araújo, M.C., Martins, J.P., Mirkhalaf, S.M., Lanceros-Mendez, S., Pires, F.M.A., Simoes, R., 2014. Predicting the mechanical behavior of amorphous polymeric materials under strain through multi-scale simulation. Appl. Surf. Sci. 306, 37–46.
Arroyo, M., Ortiz, M., 2006. Local maximum-entropy approximation schemes: a seamless bridge between finite elements and meshfree methods. Int. J. Numer. Meth. Eng. 65 (13), 2167–2202.
Bansal, M., Singh, I.V., Mishra, B., Bordas, S., 2019. A parallel and efficient multi-split XFEM for 3-D analysis of heterogeneous materials. Comput. Methods Appl. Mech. Eng. 347, 365–401.
Bauchy, M., 2017. Nanoengineering of concrete via topological constraint theory. MRS Bull. 42 (01), 50–54.
Bauchy, M., Laubie, H., Abdolhosseini Qomi, M.J., Hoover, C.G., Ulm, F.J., Pellenq, R.J. M., 2015. Fracture toughness of calcium–silicate–hydrate from molecular dynamics simulations. J. Non-Cryst. Solids 419, 58–64.
Bayesteh, H., Mohammadi, S., 2017. Micro-based enriched multiscale homogenization method for analysis of heterogeneous materials. Int. J. Solids Struct. 125, 22–42.
Beirão Da Veiga, L., Brezzi, F., Cangiani, A., Manzini, G., Marini, L.D., Russo, A., 2013. Basic principles of virtual element methods. Math. Models Methods Appl. Sci. 23 (01), 199–214.
Beltzer, A.I., 1996. Entropy characterization of finite elements. Int. J. Solids Struct. 33 (24), 3549–3560.
Bian, J., Wang, G., 2012. A multi-scale approach of amorphous polymer from coarse grain to finite element. Comput. Mater. Sci. 57, 8–13.
Bordas, S.P., Natarajan, S., 2010. On the approximation in the smoothed finite element method (SFEM). Int. J. Numer. Meth. Eng. 81 (5), 660–670.
Chakraborty, S., Natarajan, S., Singh, S., Roy, M.D., Bordas, S., 2018. Optimal numerical integration schemes for a family of polygonal finite elements with Schwarz-Christoffel conformal mapping. Int. J. Comput. Methods Eng. Sci. Mech. 19 (4), 283–304.
Chang, W.-J., Fang, T.-H., 2003. Influence of temperature on tensile and fatigue behavior of nanoscale copper using molecular dynamics simulation. J. Phys. Chem. Solids 64 (8), 1279–1283.
Chin, E.B., Lasserre, J.B., Sukumar, N., 2015. Numerical integration of homogeneous functions on convex and nonconvex polygons and polyhedra. Comput. Mech. 56 (6), 967–981.
Dehaghani, P.F., Ardakani, S.H., Bayesteh, H., Mohammadi, S., 2017. 3D hierarchical multiscale analysis of heterogeneous SMA based materials. Int. J. Solids Struct. 118, 24–40.
Demetriou, M.D., Johnson, W.L., Samwer, K., 2009. Coarse-grained description of localized inelastic deformation in amorphous metals. Appl. Phys. Lett. 94 (19), 191905.
Eidel, B., Stukowski, A., 2009. A variational formulation of the quasicontinuum method based on energy sampling in clusters. J. Mech. Phys. Solids 57 (1), 87–108.
Elliott S.R., *Physics of amorphous materials.* Longman Group, Longman House, Burnt Mill, Harlow, Essex CM 20 2 JE, England, 1983., 1983.
Ericksen, J.L., 2008. On the Cauchy—Born rule. Math. Mech. Solids 13 (3–4), 199–220.
Falk, M.L., Langer, J.S., 2011. Deformation and failure of amorphous, solidlike materials. Annu. Rev. Condens. Matter Phys. 2 (1), 353–373.
Falk, M.L., Maloney, C.E., 2010. Simulating the mechanical response of amorphous solids using atomistic methods. Eur. Phys. J. B 75 (4), 405–413.
Fan, C., Liaw, P.K., Liu, C.T., 2009. Atomistic model of amorphous materials. Intermetallics 17 (1–2), 86–87.
Fish, J., Yu, Q., 2001. Multiscale damage modelling for composite materials: theory and computational framework. Int. J. Numer. Meth. Eng. 52 (1–2), 161–191.
Fish J., *Multiscale methods: bridging the scales in science and engineering.* 2010: Oxford University Press on Demand.
Forest, S., 2002. Homogenization methods and mechanics of generalized continua-part 2. Theoret. Appl. Mech. 28–29, 113–144.
Foyouzat, A., Bayesteh, H., Mohammadi, S., 2020. A brittle to ductile phase transition fracture analysis of shape memory polymers. Eng. Fract. Mech. 224, 106751.
Foyouzat, A., Bayesteh, H., Mohammadi, S., 2021. Phase evolution based thermomechanical crack closure mechanism of shape memory polymers. Mech. Mater. 160, 103998.
France-Lanord, A., Blandre, E., Albaret, T., Merabia, S., Lacroix, D., Termentzidis, K., 2014. Atomistic amorphous/crystalline interface modelling for superlattices and core/shell nanowires. J. Phys.: Condens. Matter 26 (5), 055011.
Francis, A., Ortiz-Bernardin, A., Bordas, S.P., Natarajan, S., 2017. Linear smoothed polygonal and polyhedral finite elements. Int. J. Numer. Meth. Eng. 109 (9), 1263–1288.
Freund, L.B., Suresh S., *Thin film materials: stress, defect formation and surface evolution.* 2004: Cambridge university press.
Ghorashi, S.S., Valizadeh, N., Mohammadi, S., 2012. Extended isogeometric analysis for simulation of stationary and propagating cracks. Int. J. Numer. Meth. Eng. 89 (9), 1069–1101.
Glazov V.M. and Shchelikov O.D.J.H.T., *Volume changes during melting and heating of silicon and germanium melts.* 2000. **38**(3): p. 405-412.
Glazov, V., Shchelikov, O.D., 2000. Volume changes during melting and heating of silicon and germanium melts. High Temp. 38 (3), 405–412.
Golub, G.H., Welsch, J.H., 1969. Calculation of Gauss quadrature rules. Math. Comput. 23 (106), 221–230.
Gusev, A.A., 2017. Finite element estimates of viscoelastic stiffness of short glass fiber reinforced composites. Compos. Struct. 171, 53–62.
Hassani, B., Hinton, E., 1998. A review of homogenization and topology optimization I—homogenization theory for media with periodic structure. Comput. Struct. 69 (6), 707–717.
Hassani, B., Hinton, E., 1998. A review of homogenization and topology optimization III—topology optimization using optimality criteria. Comput. Struct. 69 (6), 739–756.
Hauseux P., Ambrosetti A., Bordas S., and Tkatchenko A., *Colossal atomic force response in van der Waals materials arising from electronic correlations.* arXiv preprint arXiv: 2106.08113, 2021.
Hauseux, P., Nguyen, T.-T., Ambrosetti, A., Ruiz, K.S., Bordas, S., Tkatchenko, A., 2020. From quantum to continuum mechanics in the delamination of atomically-thin layers from substrates. Nat. Commun. 11 (1), 1–8.
Holopainen, S., 2013. Modeling of the mechanical behavior of amorphous glassy polymers under variable loadings and comparison with state-of-the-art model predictions. Mech. Mater. 66, 35–58.
Holopainen, S., 2014. Influence of damage on inhomogeneous deformation behavior of amorphous glassy polymers. Modeling and algorithmic implementation in a finite element setting. Eng. Fract. Mech. 117, 28–50.
Holopainen, S., Barriere, T., Cheng, G., Kouhia, R., 2017. Continuum approach for modeling fatigue in amorphous glassy polymers. Applications to the investigation of damage-ratcheting interaction in polycarbonate. Int. J. Plast. 91, 109–133.
Hufnagel, T.C., Schuh, C.A., Falk, M.L., 2016. Deformation of metallic glasses: recent developments in theory, simulations, and experiments. Acta Mater. 109, 375–393.
Jahanshahi, M., Vokhshoori, M., Khoei, A., 2020. A coarse-graining approach for modeling nonlinear mechanical behavior of FCC nano-crystals. Comput. Mater. Sci. 172, 109357.
Jahanshahi, M., Ahmadi, H., Khoei, A., 2020. A hierarchical hyperelastic-based approach for multi-scale analysis of defective nano-materials. Mech. Mater. 140, 103206.
Jana, R., Savio, D., Deringer, V.L., Pastewka, L., 2019. Structural and elastic properties of amorphous carbon from simulated quenching at low rates. Modell. Simul. Mater. Sci. Eng. 27 (8), 085009.
Jia, J., Liang, Y., Tsuji, T., Murata, S., Matsuoka, T., 2016. Microscopic origin of strain hardening in methane hydrate. Sci. Rep. 6 (1), 1–10.
Jing, Y., Meng, Q., 2010. Molecular dynamics simulations of the mechanical properties of crystalline/amorphous silicon core/shell nanowires. Physica B 405 (10), 2413–2417.
Joshi, S.S., Katakam, S., Singh, A.H., Mukherjee, S., Dahotre, N.B., 2015. Amorphous coatings and surfaces on structural materials. Crit. Rev. Solid State Mater. Sci. 41 (1), 1–46.
Kahn, B.A., Fedotov, V.T., Grigoriev, A.E., Sevriukov, O.N., Pliushev, A.N., Skuratov, L. A., Polsky, V.I., Yakushin, V.L., Virgiliev, Y.S., Vasiliev, V.L., Tserevitinov, S.S., 1995. Application of amorphous filler metals in production of fusion reactor high heat flux components. Fusion Eng. Des. 28 (Supplement C), 119–124.
Kerfriden, P., Gosselet, P., Adhikari, S., Bordas, S.-P.-A., 2011. Bridging proper orthogonal decomposition methods and augmented Newton-Krylov algorithms: an adaptive model order reduction for highly nonlinear mechanical problems. Comput. Methods Appl. Mech. Eng. 200 (5–8), 850–866.
Kerfriden, P., Passieux, J.-C., Bordas, S.-P.-A., 2012. Local/global model order reduction strategy for the simulation of quasi-brittle fracture. Int. J. Numer. Meth. Eng. 89 (2), 154–179.
Kerfriden, P., Goury, O., Rabczuk, T., Bordas, S.-P.-A., 2013. A partitioned model order reduction approach to rationalise computational expenses in nonlinear fracture mechanics. Comput. Methods Appl. Mech. Eng. 256, 169–188.
Khoei, A., Jahanshahi, M., Toloui, G., 2017. Validity of Cauchy-Born hypothesis in multi-scale modeling of plastic deformations. Int. J. Solids Struct. 115, 224–247.
Khoei, A., Jahanshahi, M., 2017. Multi-scale modeling of plastic deformations in nano-scale materials; transition to plastic limit. Int. J. Numer. Meth. Eng. 109 (8), 1180–1216.
Kim, A., Medvedev, N., 2006. Melting and homogeneous crystallization of a Lennard-Jones system. J. Struct. Chem. 47 (1), S141–S150.
Kochmann, D.M., Amelang, J.S., 2016. The Quasicontinuum Method: Theory and Applications. In: Multiscale Materials Modeling for Nanomechanics. Springer, pp. 159–193.
Kronrod, A., 1965. Nodes and Weights of Quadrature Formulas: Sixteen-Place Tables. Consultants Bureau.
Kugler, S., Pusztai, L., Rosta, L., Chieux, P., Bellissent, R., 1993. Structure of evaporated pure amorphous silicon: Neutron-diffraction and reverse Monte Carlo investigations. Phys. Rev. B 48 (10), 7685.
Li, S., Liu, W.K., 1999. Reproducing kernel hierarchical partition of unity, part I—formulation and theory. Int. J. Numer. Meth. Eng. 45 (3), 251–288.
Li, S., Tong, Q.i., 2015. A concurrent multiscale micromorphic molecular dynamics. J. Appl. Phys. 117 (15), 154303.
Li, S., Urata, S., 2016. An atomistic-to-continuum molecular dynamics: theory, algorithm, and applications. Comput. Methods Appl. Mech. Eng. 306, 452–478.
Liu, L., Zhang, C., 2014. Fe-based amorphous coatings: structures and properties. Thin Solid Films 561, 70–86.
Liu, G.-R. 2009. *Meshfree Methods: Moving Beyond the Finite Element Method.* CRC Press.
Logan, R., Bond, W., 1959. Density change in silicon upon melting. J. Appl. Phys. 30 (3), 322.
Milani, G., Milani, F., 2014. Behavior of Elastomeric Seismic Isolators Varying Rubber Material and Pad Thickness: A Numerical Insight. In: Simulation and Modeling Methodologies, Technologies and Applications. Springer, pp. 55–70.

Millán, D., Sukumar, N., Arroyo, M., 2015. Cell-based maximum-entropy approximants. Comput. Methods Appl. Mech. Eng. 284, 712–731.
Millán[1] D., Amiri F., Rabczuk T., and Arroyo[1] M., *PHASE-FIELD MODELING OF FRACTURE IN THIN SHELLS WITH MAXIMUM ENTROPY APPROXIMANTS.* 2014.
Mohammadi, S. 2008. *Extended Finite Element Method: for Fracture Analysis of Structures.* John Wiley & Sons.
Moslemzadeh, H., Alizadeh, O., Mohammadi, S., 2019. Quasicontinuum multiscale modeling of the effect of rough surface on nanoindentation behavior. Meccanica 54 (3), 411–427.
Mousavi, S., Xiao, H., Sukumar, N., 2010. Generalized Gaussian quadrature rules on arbitrary polygons. Int. J. Numer. Meth. Eng. 82 (1), 99–113.
Mouton, Y. 2013. *Organic Materials in Civil Engineering.* John Wiley & Sons.
Mouton Y. 2013. *Organic Materials for Sustainable Construction.* John Wiley & Sons.
Muralidharan, K., Simmons, J., Deymier, P., Runge, K., 2005. Molecular dynamics studies of brittle fracture in vitreous silica: review and recent progress. J. Non-Cryst. Solids 351 (18), 1532–1542.
Natarajan, S., Bordas, S.P., Ooi, E.T., 2015. Virtual and smoothed finite elements: a connection and its application to polygonal/polyhedral finite element methods. Int. J. Numer. Meth. Eng. 104 (13), 1173–1199.
Nguyen, T., Ghazlan, A., Kashani, A., Bordas, S., Ngo, T., 2018. 3D meso-scale modelling of foamed concrete based on X-ray computed tomography. Constr. Build. Mater. 188, 583–598.
Nguyen, T., Kashani, A., Ngo, T., Bordas, S., 2019. Deep neural network with high-order neuron for the prediction of foamed concrete strength. Comput.-Aided Civ. Infrastruct. Eng. 34 (4), 316–332.
Norouzi, E., Moslemzadeh, H., Mohammadi, S., 2019. Maximum entropy based finite element analysis of porous media. Front. Struct. Civ. Eng. 13 (2), 364–379.
Ojovan, M.I., Louzguine-Luzgin, D.V., 2020. Revealing structural changes at glass transition via radial distribution functions. J. Phys. Chem. B 124 (15), 3186–3194.
Park, J., Han, J., Im, S., 2014. Coarse-graining of cohesive zone at interface of amorphous material. J. Mech. Sci. Technol. 28 (7), 2787–2796.
Park, E.S., Lee, J.C., Huh, M.Y., Kim, H.J., Bae, J.C., 2007. Finite element method analysis on the stress and strain states in amorphous composites containing crystalline copper during compression. Mater. Sci. Eng., A 449–451, 704–708.
Parrinello, M., Rahman, A., 1981. Polymorphic transitions in single crystals: a new molecular dynamics method. J. Appl. Phys. 52 (12), 7182–7190.
Pedone, A., Malavasi, G., Menziani, M.C., Cormack, A.N., Segre, U., 2006. A new self-consistent empirical interatomic potential model for oxides, silicates, and silica-based glasses. J. Phys. Chem. B 110 (24), 11780–11795.
Pedone, A., Malavasi, G., Menziani, M.C., Segre, U., Cormack, A.N., 2008. Molecular dynamics studies of stress– strain behavior of silica glass under a tensile load. Chem. Mater. 20 (13), 4356–4366.
Rappel, H., Beex, L.A., Noels, L., Bordas, S., 2019. Identifying elastoplastic parameters with Bayes' theorem considering output error, input error and model uncertainty. Probab. Eng. Mech. 55, 28–41.
Rappel H., Beex L.A., Hale J.S., Bordas S. 2016. *Bayesian inference for the stochastic identification of elastoplastic material parameters: introduction, misconceptions and insights.* arXiv preprint arXiv:1606.02422.
Rinaldi, R., Gaertner, R., Chazeau, L., Gauthier, C., 2011. Modelling of the mechanical behaviour of amorphous glassy polymer based on the Quasi Point Defect theory—Part I: Uniaxial validation on polycarbonate. Int. J. Non Linear Mech. 46 (3), 496–506.
Rinaldi, R., Gaertner, R., Brunet, M., Chazeau, L., Vidal-Sallé, E., Gauthier, C., 2011. Modeling of the mechanical behavior of amorphous glassy polymer based on the quasi-point defect theory—Part II: 3D formulation and finite element modeling of polycarbonate. Int. J. Non Linear Mech. 46 (3), 507–518.
Sanchez, C., Livage, J., Audiere, J., Madi, A., 1984. Influence of the quenching rate on the properties of amorphous V_2O_5 thin films. J. Non-Cryst. Solids 65 (2–3), 285–300.
Sasaki, H., Tokizaki, E., Terashima, K.T.K., Kimura, S.K.S., 1994. Density variation of molten silicon measured by an improved archimedian method. Jpn. J. Appl. Phys. 33 (7R), 3803.
Shannon, C.E. 2001. *A mathematical theory of communication.* ACM SIGMOBILE mobile computing and communications review, **5**(1), 3-55.
Shenoy, V., Miller, R., Tadmor, E., Rodney, D., Phillips, R., Ortiz, M., 1999. An adaptive finite element approach to atomic-scale mechanics—the quasicontinuum method. J. Mech. Phys. Solids 47 (3), 611–642.
Shi, Y., Falk, M.L., 2006. Atomic-scale simulations of strain localization in three-dimensional model amorphous solids. Phys. Rev. B 73 (21).
Shi, Y., Falk, M.L., 2007. Simulations of nanoindentation in a thin amorphous metal film. Thin Solid Films 515 (6), 3179–3182.
Shodja, H.M., Tabatabaei, M., Esfarjani, K., 2014. First principles molecular dynamics studies of elastic constants, ideal tensile strength, chemistry of crack initiation, and surface and cohesive energies in amorphous silicon. Philos. Mag. 94 (25), 2913–2936.
Stillinger, F.H., Weber, T.A., 1985. Computer simulation of local order in condensed phases of silicon. Phys. Rev. B 31 (8), 5262.
Su, Z.C., Tay, T.-E., Chen, Y.U., Tan, V.B.C., 2012. Multiscale modeling for amorphous materials — Mapping atomistic displacements to macroscopic deformation. Int. J. Appl. Mech. 04 (04), 1250037.
Su, Z.C., Tan, V.B.C., Tay, T.E., 2012. Concurrent multiscale modeling of amorphous materials in 3D. Int. J. Numer. Meth. Eng. 92 (13), 1081–1099.
Su, Z.C., Tan, V.B.C., Tay, T.E., 2014. 3D multiscale simulation of a silicon slider on a PE substrate. Comput. Mater. Sci. 94, 240–244.
Sukumar, N., 2004. Construction of polygonal interpolants: a maximum entropy approach. Int. J. Numer. Meth. Eng. 61 (12), 2159–2181.
Sukumar, N., 2013. Quadratic maximum-entropy serendipity shape functions for arbitrary planar polygons. Comput. Methods Appl. Mech. Eng. 263, 27–41.
Tabarraei, A., Sukumar, N., 2008. Extended finite element method on polygonal and quadtree meshes. Comput. Methods Appl. Mech. Eng. 197 (5), 425–438.
Tadmor, E.B., Miller R.E. 2011. *Modeling Materials: Continuum, Atomistic and Multiscale Techniques.* Cambridge University Press.
Tadmor, E.B., Ortiz, M., Phillips, R., 1996. Quasicontinuum analysis of defects in solids. Philos. Mag. A 73 (6), 1529–1563.
Talebi, H., Silani, M., Bordas, S., Kerfriden, P., Rabczuk, T., 2014. A computational library for multiscale modeling of material failure. Comput. Mech. 53 (5), 1047–1071.
Tan, V.B.C., Zeng, X.S., Deng, M., Lim, K.M., Tay, T.E., 2008. Multiscale modeling of polymers – The pseudo amorphous cell. Comput. Methods Appl. Mech. Eng. 197 (6–8), 536–554.
Telford, M., 2004. The case for bulk metallic glass. Mater. Today 7 (3), 36–43.
Timmel, M., Kolling, S., Osterrieder, P., Du Bois, P.A., 2007. A finite element model for impact simulation with laminated glass. Int. J. Impact Eng. 34 (8), 1465–1478.
Urata, S., Li, S., 2017. A multiscale model for amorphous materials. Comput. Mater. Sci. 135, 64–77.
Vu-Bac, N., Bessa, M., Rabczuk, T., Liu, W.K., 2015. A multiscale model for the quasi-static thermo-plastic behavior of highly cross-linked glassy polymers. Macromolecules 48 (18), 6713–6723.
Wagner, G.J., Liu, W.K., 2003. Coupling of atomistic and continuum simulations using a bridging scale decomposition. J. Comput. Phys. 190 (1), 249–274.
Wang, J., Hodgson, P.D., Zhang, J., Yan, W., Yang, C., 2009. Effects of quenching rate on amorphous structures of Cu46Zr54 metallic glass. J. Mater. Process. Technol. 209 (9), 4601–4606.
Wang, G., Huang, Z., Xiao, P., Zhu, X., 2016. Spraying of Fe-based amorphous coating with high corrosion resistance by HVAF. J. Manuf. Processes 22, 34–38.
Wang, W., Zhang, C., Zhang, Z.W., Li, Y.C., Yasir, M., Wang, H.T., Liu, L., 2017. Toughening Fe-based amorphous coatings by reinforcement of amorphous carbon. Sci. Rep. 7 (1), 4084.
Xiao, S., Belytschko, T., 2004. A bridging domain method for coupling continua with molecular dynamics. Comput. Methods Appl. Mech. Eng. 193 (17–20), 1645–1669.
Yuan, F., Huang, L., 2012. Molecular dynamics simulation of amorphous silica under uniaxial tension: from bulk to nanowire. J. Non-Cryst. Solids 358 (24), 3481–3487.
Zaccone, A., 2009. The shear modulus of metastable amorphous solids with strong central and bond-bending interactions. J. Phys.: Condens. Matter 21 (28), 285103.
Zaccone, A., Scossa-Romano, E., 2011. Approximate analytical description of the nonaffine response of amorphous solids. Phys. Rev. B 83 (18).
Zhao, J., Lu, L., Rabczuk, T., 2015. The tensile and shear failure behavior dependence on chain length and temperature in amorphous polymers. Comput. Mater. Sci. 96, 567–572.
Zhou, X., Zhou, H., Li, X., Chen, C., 2015. Size effects on tensile and compressive strengths in metallic glass nanowires. J. Mech. Phys. Solids 84, 130–144.